Article

Cell Reports

Transcription Factor NFIB Is a Driver of Small Cell Lung Cancer Progression in Mice and Marks Metastatic Disease in Patients

Graphical Abstract

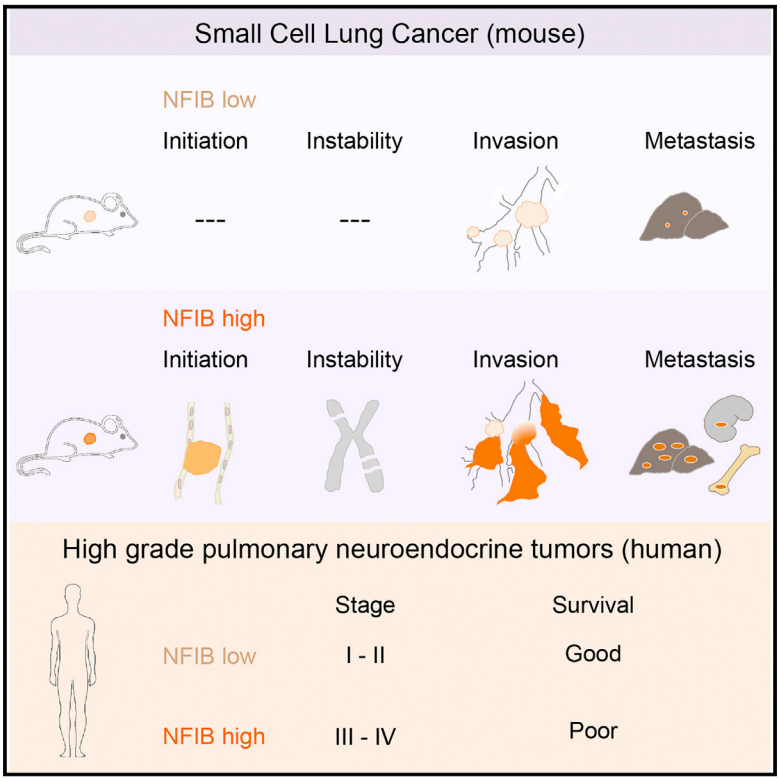

Authors

Ekaterina A. Semenova, Min-chul Kwon, Kim Monkhorst, ..., Arno Velds, Ivo J. Huijbers, Anton Berns

Correspondence

i.huijbers@nki.nl (I.J.H.), a.berns@nki.nl (A.B.)

In Brief

SCLC is a highly malignant cancer with an unmet need for better intervention strategies. Semenova et al. report that the transcription factor NFIB drives SCLC growth and metastasis, defines an aggressive tumor compartment in mice, and marks a subgroup of high-grade pulmonary neuroendocrine tumors (pNETs) in patients.

Highlights

- NFIB drives tumor initiation and progression in mouse models of SCLC
- NFIB enhances metastasis and changes the metastatic profile
- NFIB promotes dedifferentiation and invasion in SCLC
- NFIB marks stage III/IV high-grade neuroendocrine carcinomas in patients

Accession Numbers

GSE82005

Semenova et al., 2016, Cell Reports *16*, 631–643
July 19, 2016
http://dx.doi.org/10.1016/j.celrep.2016.06.020

Cell Reports
Article

Transcription Factor NFIB Is a Driver of Small Cell Lung Cancer Progression in Mice and Marks Metastatic Disease in Patients

Ekaterina A. Semenova,[1,10] Min-chul Kwon,[1,10] Kim Monkhorst,[2,10] Ji-Ying Song,[3] Rajith Bhaskaran,[1,8] Oscar Krijgsman,[5] Thomas Kuilman,[5] Dennis Peters,[4] Wieneke A. Buikhuisen,[6] Egbert F. Smit,[6] Colin Pritchard,[7] Miranda Cozijnsen,[1] Jan van der Vliet,[1] John Zevenhoven,[1] Jan-Paul Lambooij,[1] Natalie Proost,[1] Erwin van Montfort,[1] Arno Velds,[8] Ivo J. Huijbers,[7,11,*] and Anton Berns[1,9,11,*]
[1]Division of Molecular Genetics
[2]Division of Pathology
[3]Division of Experimental Animal Pathology
[4]Core Facility for Molecular Pathology and Biobanking
[5]Division of Molecular Oncology
[6]Division of Thoracic Oncology
[7]Mouse Clinic for Cancer and Aging research Transgenic Core Facility
[8]Genomics Core Facility
The Netherlands Cancer Institute, Amsterdam 1066 CX, the Netherlands
[9]Skolkovo Institute of Science and Technology, Moscow 143026, Russia
[10]Co-first author
[11]Co-senior author
*Correspondence: i.huijbers@nki.nl (I.J.H.), a.berns@nki.nl (A.B.)
http://dx.doi.org/10.1016/j.celrep.2016.06.020

SUMMARY

Small cell lung cancer (SCLC) is an aggressive neuroendocrine tumor, and no effective treatment is available to date. Mouse models of SCLC based on the inactivation of *Rb1* and *Trp53* show frequent amplifications of the *Nfib* and *Mycl* genes. Here, we report that, although overexpression of either transcription factor accelerates tumor growth, NFIB specifically promotes metastatic spread. High NFIB levels are associated with expansive growth of a poorly differentiated and almost exclusively E-cadherin (CDH1)-negative invasive tumor cell population. Consistent with the mouse data, we find that NFIB is overexpressed in almost all tested human metastatic high-grade neuroendocrine lung tumors, warranting further assessment of NFIB as a tumor progression marker in a clinical setting.

INTRODUCTION

Small cell lung cancer (SCLC) is the most aggressive subtype of lung cancer and is characterized by early metastatic spread to multiple organs (Byers and Rudin, 2015). It is most often diagnosed at an advanced stage of disease and is generally fatal within 4 months if left untreated. Another striking feature of SCLC is its exceptional initial response to standard first line chemotherapy regimens, which is followed by rapid relapse of chemoresistant tumors, limiting the survival benefit for SCLC patients (Byers and Rudin, 2015). The results of numerous clinical trials testing distinct therapeutic approaches for SCLC have been disappointing, and treatment programs have not changed in the last three decades (Byers and Rudin, 2015). Due to its metastatic nature at presentation, SCLC is rarely resected, leading to a scarcity of tumor material for analysis. In this context, mouse models of SCLC provide a powerful tool to study the biology of SCLC initiation, progression, and mechanisms of resistance (Kwon and Berns, 2013).

We have previously generated a mouse model of SCLC based on conditional inactivation of the tumor suppressor genes, *Trp53* and *Rb1*, both of which are deleted in nearly all human SCLC cases (George et al., 2015; Meuwissen et al., 2003). The model recapitulates many salient features of SCLC, including its localization, metastatic progression, and histopathological characteristics (Gazdar et al., 2015; Meuwissen et al., 2003). In this model, recurrent genetic alterations included losses on chromosomes 8, 12, 14, 16, and 19 and both gains and losses on chromosome 4 (Dooley et al., 2011; McFadden et al., 2014). They likely provide a selective advantage to tumor cells during tumor evolution and may harbor driver genes in case of gene amplification. Chromosome 4 in particular often shows a number of genomic alterations such as focal deletions encompassing *miR200a/miR200b*, the hairy enhancer of split family of transcription factors (*Hes2*, *Hes3*, and *Hes5*), *Trp73*, and two focal amplifications, one encompassing *Mycl* and another *Nfib* (Calbo et al., 2011; McFadden et al., 2014).

MYCL is a basic-helix-loop-helix transcription factor reported to be an oncogene in SCLC. Several studies applying exome and whole genome sequencing reported recurrent amplification of the *MYC* family of oncogenes, including *MYCL* in SCLC

(6.9%–9%) (Calbo et al., 2011; George et al., 2015; Iwakawa et al., 2013). In line with this observation, targeted overexpression of *Mycl* in a mouse model vastly accelerated tumor development (Huijbers et al., 2014).

NFIB belongs to the nuclear factor 1 (NFI) family of transcription factors. They were found as factors essential for adenovirus replication, but are now known to control expression of a large number of cellular genes (Gronostajski, 2000; Harris et al., 2015). The four members in vertebrates, NFIA, NFIB, NFIC, and NFIX, can bind as hetero and homodimers to the TTGGC(N5)GCCAA dyad symmetric consensus sequence and either activate or repress transcription depending on the context (Harris et al., 2015). They are expressed in multiple organ systems in partially overlapping patterns and play an important role in regulating tissue-specific expression programs (Harris et al., 2015). NFIB regulates proliferation and epithelial differentiation during lung maturation, and NFIB knockout animals have severe lung hypoplasia and developmental defects in the brain (Hsu et al., 2011; Steele-Perkins et al., 2005). In addition, it was reported to coordinate epithelial-melanocyte stem cell proliferation and differentiation in hair follicles, where it was shown to regulate the expression of 1,449 target genes (Chang et al., 2013). In the brain, NFIB regulates the differentiation of neural progenitor cells (Piper et al., 2014).

Several reports have defined NFIB as an oncogene (Dooley et al., 2011; Zhang et al., 2015). The chromosomal region encoding NFIB is amplified in patients with triple-negative breast cancer (Han et al., 2008), in patients with squamous cell carcinoma of the esophagus (Yang et al., 2001), and in submandibular gland carcinoma (Andreasen et al., 2016). Increased NFIB levels are also found in metastatic giant cell tumors of bone and are associated with an elevated risk of metastasis (Mosakhani et al., 2013; Quattrini et al., 2015). Using SCLC cell lines from both patients and mouse models, NFIB was shown to regulate apoptosis, senescence, and proliferation and to allow for anchorage-independent growth of fibroblasts (Dooley et al., 2011).

In contrast to *MYC* family genes, *NFIB* is amplified in a very limited number of human SCLC cases (George et al., 2015; Iwakawa et al., 2013). Considering the high frequency of its focal amplification in mouse, and its oncogenic potential in vitro, we decided to test how NFIB expression affects SCLC development in vivo and to examine its potential role in human SCLC.

RESULTS

NFIB Accelerates SCLC Initiation and Progression

To assess the role of NFIB in driving SCLC, we generated two transgenic mouse strains that overexpressed *Nfib* concomitant with *Trp53* and *Rb1* loss, one expressing full-length *Nfib* (variant 1) and the other a shorter *Nfib* version lacking exons 9–11 (variant 3) (Figure S1A). Both variants contain the conserved DNA binding domain; however, the shorter one lacks a putative proline-rich transactivation domain at the C terminus (Gronostajski, 2000; Mermod et al., 1989). Both are expressed in normal mouse lung and in SCLC tumors of the *Rb1*$^{F/F}$;*Trp53*$^{F/F}$ mouse model (Figure S1B). The targeted transgenes allowed for expression of the transgenic *Nfib* and firefly *Luciferase* (*Luc*) upon CRE mediated inversion (Figure S1C). Mouse models carrying similar targeted transgenes for either *Mycl-Luc* or *Luc* have been described previously (Huijbers et al., 2014). Four cohorts of animals were generated and analyzed in parallel as follows: (1) a control cohort of *Rb1*$^{F/F}$;*Trp53*$^{F/F}$ and *invCAG-Luc;Rb1*$^{F/F}$;*Trp53*$^{F/F}$ mice, (2) a Mycl cohort of *invCAG-Mycl-Luc;Rb1*$^{F/F}$;*Trp53*$^{F/F}$ mice, (3) an Nfib cohort of *invCAG-Nfib_v1-Luc;Rb1*$^{F/F}$;*Trp53*$^{F/F}$ and *invCAG-Nfib*_v3-*Luc;Rb1*$^{F/F}$;*Trp53*$^{F/F}$ mice, and (4) an Nfib/Mycl cohort generated by crossbreeding of *invCAG-Nfib_v1-Luc;Rb1*$^{F/F}$;*Trp53*$^{F/F}$ with *invCAG-Mycl-Luc;Rb1*$^{F/F}$;*Trp53*$^{F/F}$ animals. The Nfib cohort contained both Nfib variants, since no significant differences were observed between them with regard to the parameters analyzed in this study. The Nfib/Mycl cohort was included to test whether NFIB can augment SCLC progression in combination with the strong oncogene MYCL and to gain insight into the selective pressure conferred by the frequent co-occurrence of *Nfib* and *Mycl* amplifications. All animals were injected intra-tracheally with adenovirus carrying the CRE recombinase driven from the ubiquitous CMV promoter. CRE expression resulted in the deletion of *Trp53* and *Rb1* and transcriptional activation of the transgenes (Figure S1D).

To monitor the dynamics of tumor development, we used bioluminescence imaging (Figures 1A and 1B). Control and Nfib cohort animals exhibited a similar tumor growth pattern, with a minimal increase in signal during the first weeks followed by a sharp switch to exponential growth. This switch occurred earlier in the Nfib cohort (median of 175 days) than in the control cohort (median at 201 days) (Figures 1A and 1B). In contrast, animals in both Mycl and Nfib/Mycl cohorts showed an exponential increase in the signal soon after its first detection with a median switch time of 109 and 89 days for Mycl and Nfib/Mycl, respectively (Figures 1A and 1B). The pattern of luciferase signal directly correlated with survival in the four cohorts (Figure 1C). Animals in the control group had the longest latency with a median of 235 days. NFIB overexpressing animals had a significantly decreased tumor latency (median survival of 193 days), with the two transcript variants in the Nfib cohort showing indistinguishable tumor acceleration when analyzed separately (Figure S1E). Mycl animals had decreased tumor latency as compared to both the control and Nfib mice (median latency of 146 days). A combination of NFIB and MYCL overexpression decreased tumor latency further to a median of 132 days. Therefore, NFIB and MYCL co-expression enhances SCLC development, consistent with their frequent co-amplification in mouse SCLC (Dooley et al., 2011).

To characterize the early stages of tumor formation, we sacrificed animals at distinct time points post-virus injection, starting at 70 days. Based on the luciferase signal, we did not expect any lesions in control and Nfib animals at that stage and expected some initial lesions in Mycl and Nfib/Mycl animals. Therefore, we included only one Mycl and one Nfib/Mycl mouse at this time point. Indeed, most of the lung was normal in both genotypes, with only four small hyperplastic lesions in each (Figures 1D, S2A, and S2B). We next collected lungs from animals in all groups 98 days following virus injection. No lesions were identified in the control cohort (three mice), and one lesion was found in one out of three lungs of the Nfib cohort. In contrast, both Mycl

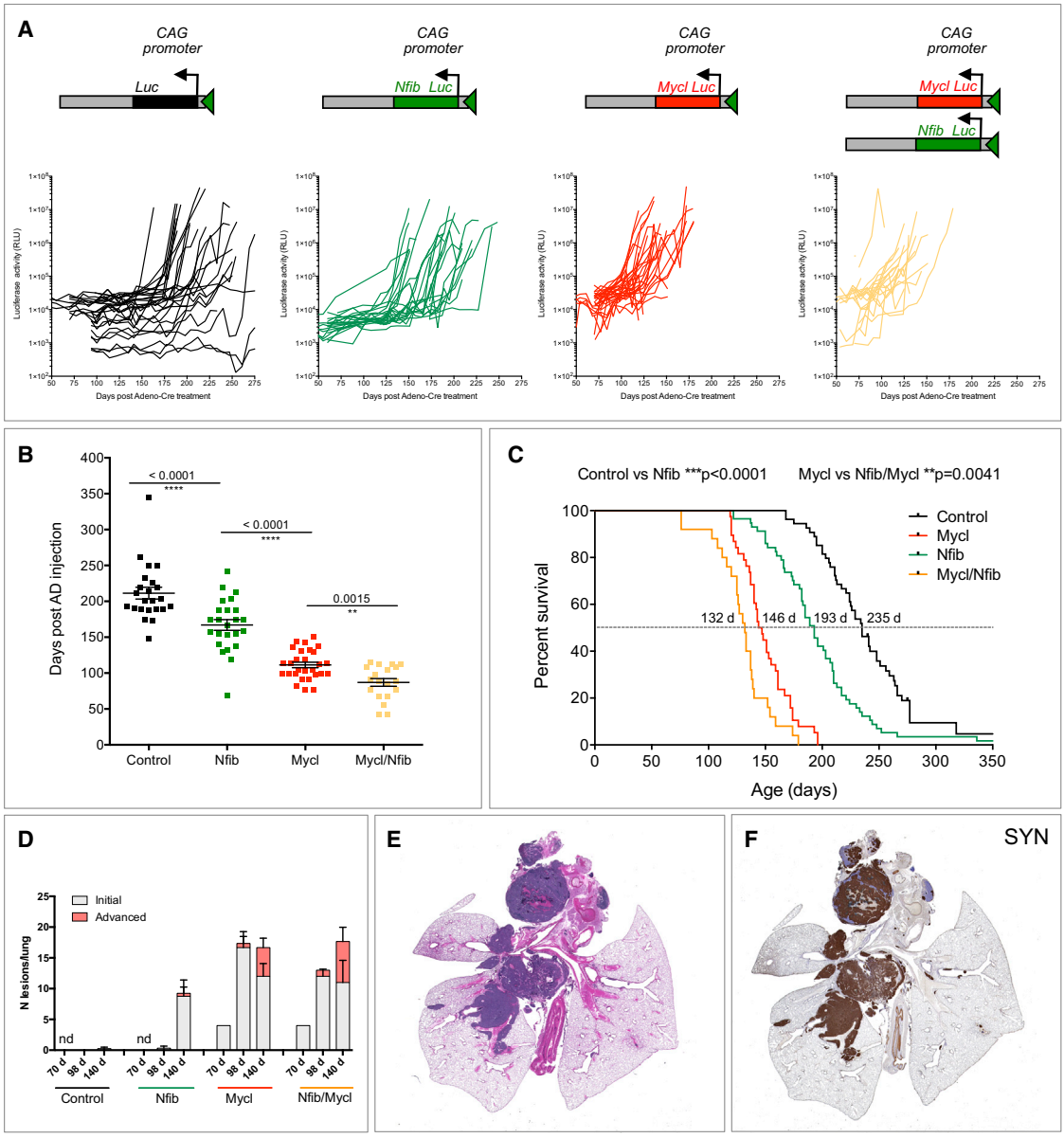

Figure 1. NFIB Accelerates Tumor Initiation and Progression in a Mouse Model of SCLC

(A) Schematic representation of the switched targeted transgene and measurements of luciferase activity from thorax over time following viral induction.

(B) Time point (in days) at which linear growth switched to exponential growth based on luciferase signal.

(C) Survival curves of animals within the four cohorts.

(D) Quantification of lesions (initial and advanced) at 70, 98, and 140 days following viral induction.

(E) A representative H&E staining of advanced lung lesions (taken from the control cohort, 193 days post-induction).

(F) Synaptophysin (SYN) staining of the same lung as in (E).

Error bars in (B) and (D) represent mean ± SEM.

See also Figures S1, S2, and S3.

and Nfib/Mycl cohorts had multiple initial lesions (average 16.7 and 12 in Mycl and Nfib/Mycl, respectively, 3 lungs each). In addition, one Mycl lung and all three Nfib/Mycl lungs contained one or two advanced lesions (Figures 1D, S2C, and S2D). At 140 days following tumor induction, our final collection time point, animals in the control cohort showed minimal evidence of tumor initiation (a single lesion in one out of four lungs) (Figure 1D). In contrast, the Nfib cohort contained multiple initial lesions (average of 8.3, four lungs), and one out of four lungs contained two advanced lesions (Figure 1D). At the same time point, both Mycl and Nfib/Mycl animals had multiple initial and advanced lesions, with an average of 12 initial and 4.7 advanced for Mycl, and 11 initial and 7 advanced for Nfib/Mycl (Figures 1D, S2E, and S2F). Initial lesions in the control cohort became

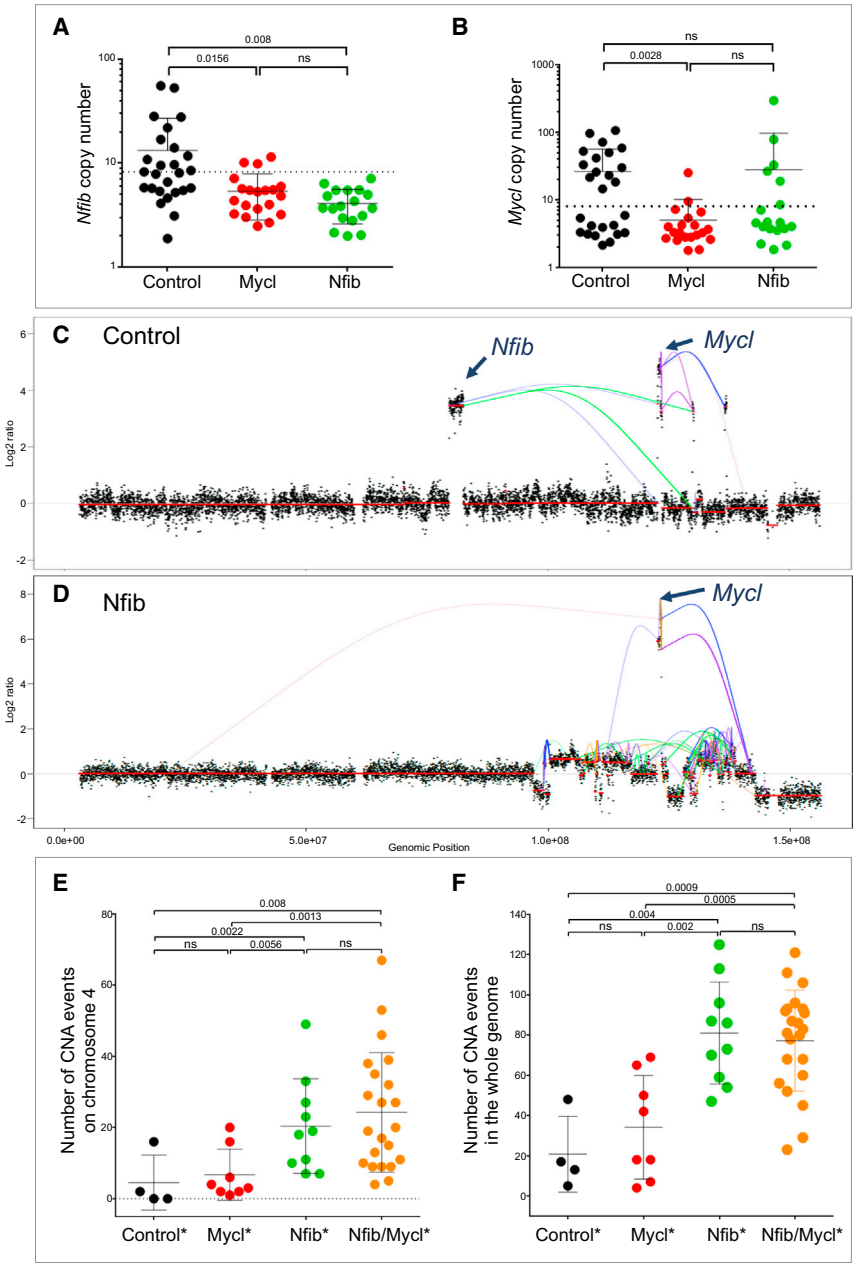

Figure 2. NFIB Is Associated with Increased Chromosomal Instability

(A and B) Copy number of *Nfib* (A) and *Mycl* (B) genomic locus in control, Mycl, and Nfib cohort tumors. The dotted line indicates the threshold.

(C and D) Genomic rearrangement and copy-number alterations on chromosome 4 in control (C) and Nfib (D) tumors. Line coloring indicates orientation of fusion ends.

(E and F) Total number of copy-number aberration (CNA) events on chromosome 4 (E) and in the whole genome (F) in different tumor classes (indicated by *). Copy-number gain (log2 ratio > 0.459) and loss (log2 ratio < −0.67).

Data are mean ± SEM.

evident at 175 days post-injection (data not shown). Thus, overexpression of *Nfib* accelerated tumor initiation by 5 weeks, while overexpression of *Mycl* and *Nfib/Mycl* accelerated tumor initiation by 15 weeks.

We next performed a detailed histological evaluation of animals sacrificed due to respiratory distress. Full necropsy was carried out, and tissues were sectioned and stained with H&E. A range of lesions from atypical hyperplasia and intraepithelial neoplasia to advanced SCLC were identified in lung sections from animals in all groups. They were mainly located in the central lung and frequently within the mediastinum (Figure 1E). Peripheral lesions within the alveolar compartment were also found. Next, we stained lung sections with markers of neuroendocrine (NE) differentiation (synaptophysin, chromogranin, NCAM, and CGRP). All lesions were positive for these markers, confirming their NE origin (Figure 1F; data not shown). Interestingly, 10 out of 29 of the Nfib/Mycl animals and 4 out of 26 of the Nfib animals developed NE tumors within the trachea (Figures S3A–S3C). This was evident from both the luciferase imaging and histological evaluation (Figures S3A and S3B). This phenotype was driven by NFIB, as none of the Mycl mice (0 out of 32) had tumors in the trachea (Figure S3C). Interestingly, while NE cells within the central lung are mostly found in clusters (neuroendocrine bodies), NE cells in the trachea appear as single cells (Figures S3D and S3E).

Thus NFIB significantly accelerated tumor initiation and progression in the lung and supported tumor induction at a novel location, the trachea.

NFIB Is Associated with Chromosomal Instability

Focal amplifications of *Nfib* are frequently observed in mouse SCLC model (Dooley et al., 2011). However, other genes located near the *Nfib* locus are often co-amplified, e.g., *Tyrp1*, *Mpdz*, *Cer1*, *Frem1*, *Zdhhc21*, and *Psip1*, some of which have previously been implicated in tumor development (Cermáková et al., 2014; French et al., 2016; Ghanem and Fabrice, 2011). To examine whether transgenic *Nfib* expression is sufficient to eliminate the selective pressure for amplification of the corresponding endogenous locus, the copy number of *Nfib* in tumors from Nfib mice was examined using qPCR (Figures 2A and 2B). Previously we showed that the *Mycl* locus is not amplified in 95% of tumors of Mycl mice, arguing that the *Mycl* transgene abrogates the requirement for its amplification (Figure 2B) (Huijbers et al., 2014). Similarly, all tumors driven by the *Nfib* transgene exhibited

Table 1. Classes Based on Status of *Nfib* and *Mycl* in the Tumor

Class	Mouse Genotype (*Rb1*$^{F/F}$;*P53*$^{F/F}$; *invCAG*-)	Tumor Genotype (Endogenous Locus)		Tumor Expression (qPCR Relative to Normal Lung)
Control[a]	*Luc* (or WT)	*Nfib* and *Mycl* normal	and/or	*Nfib* and *Mycl* normal
Nfib[a]	*Nfib-Luc*			
	Luc (or WT)	*Nfib*, copies > 8	and/or	*Nfib*, REU > 8
Mycl[a]	*Mycl-Luc*			
	Luc (or WT)	*Mycl*, copies > 8	and/or	*Mycl*, REU > 100
Nfib/ Mycl[a]	*Nfib-Luc; Mycl-Luc*			
	Nfib-Luc	*Mycl*, copies > 8	and/or	*Mycl*, REU > 100
	Mycl-Luc	*Nfib*, copies > 8	and/or	*Nfib*, REU > 8
	Luc (or WT)	*Mycl*, copies > 8 and *Nfib*, copies > 8	and/or	*Mycl*, REU > 100 and *Nfib*, REU > 8

[a]Indicates tumor class in figures. WT, wild type; REU, relative expression units.

a normal DNA copy number of the endogenous *Nfib* locus (Figures 2A and 2B). In combination with the accelerated SCLC tumor growth, this formally proves that *Nfib* is a bona fide driver of SCLC.

Amplification of the *Mycl* locus was detected in 33% of tumors in Nfib mice (6 out of 18 tumors). Conversely, the *Nfib* locus was amplified in 3 out of 20 tumors (15%) in Mycl mice (Figures 2A and 2B). These amplifications are in line with the reduced tumor latency observed in the Nfib/Mycl cohort and support a selective benefit for co-expression of *Nfib* and *Mycl* in SCLC. In control tumors, concurrent amplification of *Nfib* and *Mycl* is observed in 35% (9 out of 26) of cases (Figures 2A and 2B). These co-amplifications are striking, since both genes are never part of the same amplicon despite being juxtaposed on chromosome 4 (40.6 Mb apart). To gain better insight into the mechanism of co-amplification, we performed mate-pair sequencing on tumors of control and Nfib mice (Figures 2C and 2D). The tumors showed focal amplifications on chromosome 4, including *Nfib* and/or *Mycl* loci. We observed intrastrand chromosomal rearrangements leading to a re-shuffle of the chromosome in three out of five tumors examined. This type of intrastrand rearrangements was only observed on chromosome 4. This suggests that these rearrangements frequently occur simultaneously and are likely the result of a single catastrophic event, in line with several case reports for human SCLC (George et al., 2015; Iwakawa et al., 2013; Stephens et al., 2011). Observed amplifications likely reflect clonal evolution causing the heterogeneity we describe below.

To obtain an estimate of the overall genomic stability in SCLC in our mouse models, low-coverage whole genome sequencing was performed on a panel of tumors. The tumors were divided into different classes based on the type of transgene, on the focal amplification of either the *Nfib* or *Mycl* locus, and on their expression (Table 1). This division into classes allowed us to link genomic aberrations to gene expression of *Nfib* alone (Nfib class), *Mycl* alone (Mycl class), or both (Nfib/Mycl class). Both control and Mycl class tumors had a limited number of copy-number aberrations (CNAs). Surprisingly, Nfib class tumors showed a significantly increased number of CNA events compared to control and Mycl class tumors, and these chromosomal rearrangements were widely spread over the genome and chromosome 4 (Figures 2E and 2F). Interestingly, we also observed an increase in the number of CNA events when comparing Nfib/Mycl to Mycl class, suggesting that chromosomal instability is specifically associated with *Nfib* overexpression (Figures 2E and 2F).

NFIB Changes the Metastatic Profile

One of the key characteristics of SCLC is its aggressive metastatic dissemination. We therefore asked whether *Nfib* overexpression affected metastatic behavior of SCLC cells. The original *Trp53;Rb1* SCLC mouse model primarily shows metastasis to the liver (Meuwissen et al., 2003). We stained livers with NCAM antibody to identify NE metastatic lesions and quantified the number of animals that carried liver metastasis within each of the four classes (Table 1). Considering the prevalence of upper airway lesions and associated early lethality, which likely prevented full metastatic dissemination, animals carrying both *Nfib* and *Mycl* transgenes were excluded from the analysis. Only 1 out of 7 animals and 3 out of 13 animals in the control and Mycl class, respectively, showed liver metastasis (Figure 3A). In contrast, the majority of animals in the two Nfib containing classes had liver metastases. Specifically, 8 out of 10 Nfib class animals and 17 out of 21 Nfib/Mycl class animals had multiple metastases in the liver (Figure 3A). Further characterization of liver samples revealed that some livers contained only a few foci, while others showed massive colonization by NCAM-positive cells. Also, metastatic foci themselves varied in size. Therefore, we quantified both the number of foci and the relative area of the liver occupied by metastases (Figures 3B and 3C). Control class animals had on average 1.5 ± 1.5 and Mycl class animals had 1 ± 0.6 metastatic foci per liver section. In contrast, Nfib class animals contained on average 9.7 ± 3 foci and Nfib/Mycl class animals 31 ± 10 foci per liver section (Figure 3B). The two *Nfib* isoforms showed a similar pattern (Figure S4A). Also, the area covered by liver metastases was significantly higher within the two Nfib containing classes when compared to both control and Mycl classes (Figure 3C). Importantly, all the liver samples with the highest metastatic load belonged to Nfib/Mycl class, while animals in the Nfib and Mycl classes had on average an intermediate and low tumor load, respectively (Figures 3B–3F).

NFIB also changed the metastatic profile. We noted metastases to kidney and bone (Figures 3G, S4B, and S4C). All these cases belonged to either the Nfib or Nfib/Mycl class (Figures 3B, 3C, and 3H). In all instances, metastases were exclusively composed of NE cells as judged by SYN and NCAM staining and their morphology (Figures 3D–3F; data not shown). Thus, NFIB promotes more extensive metastasis in the SCLC mouse model.

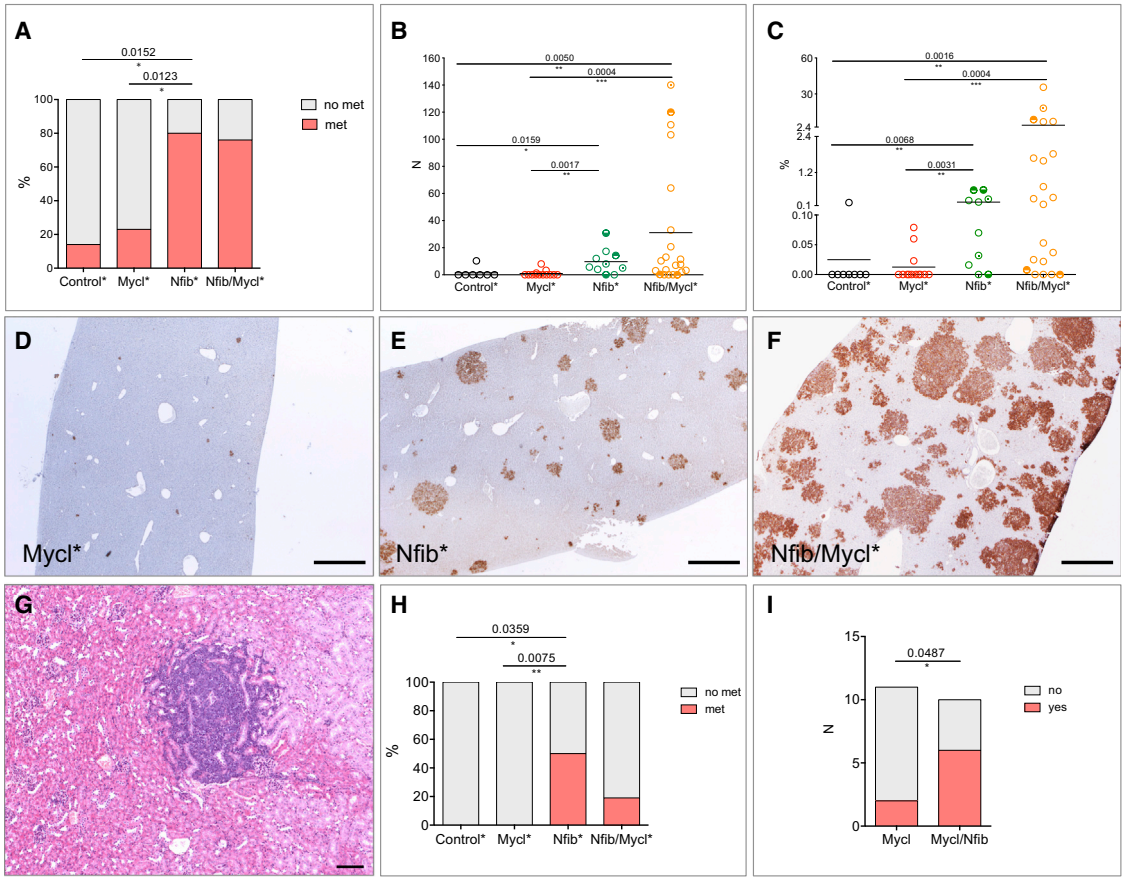

Figure 3. NFIB Promotes Metastases and Changes the Metastatic Profile

(A) Percent of animals with and without liver metastasis in each of the four classes.

(B) Quantification of the number of liver metastasis in each class.

(C) Quantification of the percent area of the liver covered by metastatic lesions in each of the four classes. Circles with a shaded upper or lower half indicate animals with kidney and bone metastasis, respectively. Circles marked with a central dot indicate animals with metastasis to both kidney and bone.

(D–F) Representative liver section from the three classes, Mycl (D), Nfib (E), and Nfib/Mycl (F), stained with NCAM to identify NE metastatic lesions.

(G) NE metastasis in the kidney, H&E.

(H) Percent of animals in each class with metastatic lesions outside the liver (bone, kidney).

(I) Number of animals in Mycl and Nfib/Mycl cohort that provided successful culture of NE cells from the blood.

Scale bars in (D)–(F), 200 μm. Scale bar in (G) represents 100 μm. See also Figure S4.

The transgenic Nfib/Mycl cohort showed a relatively low incidence of metastasis (7 out of 28 animals) (data not shown). To test whether, despite early lethality and presence of upper airway lesions, NFIB also conferred metastatic potential in the transgenic Nfib/Mycl cohort, we looked for the presence of circulating tumor cells as a surrogate indicator of metastasis. In the absence of a suitable surface marker that would allow us to reliably quantify these cells, we collected blood from animals in Mycl and Nfib/Mycl cohorts and initiated cultures using media that supports growth of NE cells. The success rate of culturing NE cells was significantly higher in Nfib/Mycl cohort animals (6 out of 10), as compared to Mycl cohort animals (2 out of 11) (Figure 3I). One of the two Mycl animals that did exhibit growth from circulating tumor cells showed Nfib overexpression (20-fold increase by qPCR), indicating that it actually should be counted as belonging to the Nfib/Mycl class in this assay (data not shown). Therefore, NFIB is supporting metastasis of the tumor cells by promoting their intravasation, their survival, or both at early stages of dissemination.

NFIB Activates a Migration and Survival Program

In order to identify the putative targets of NFIB and to understand its role in tumor development and metastasis, we established SCLC cell lines from Mycl cohort tumors with low NFIB expression. We overexpressed mouse *Nfib* in four of these cell lines to examine the differential gene expression profiles (Figures S5A–S5C). We observed 148 upregulated and 70 downregulated genes following NFIB overexpression (Figure 4A; Table S1). To identify the signaling networks likely responsible for driving tumor progression, we performed functional clustering analysis of the differentially expressed genes using the Ingenuity Pathway Analysis. Analysis of upregulated genes showed significant enrichment for cellular growth and proliferation, cellular movement, and cell death and survival pathways (Figure 4B). 46 out

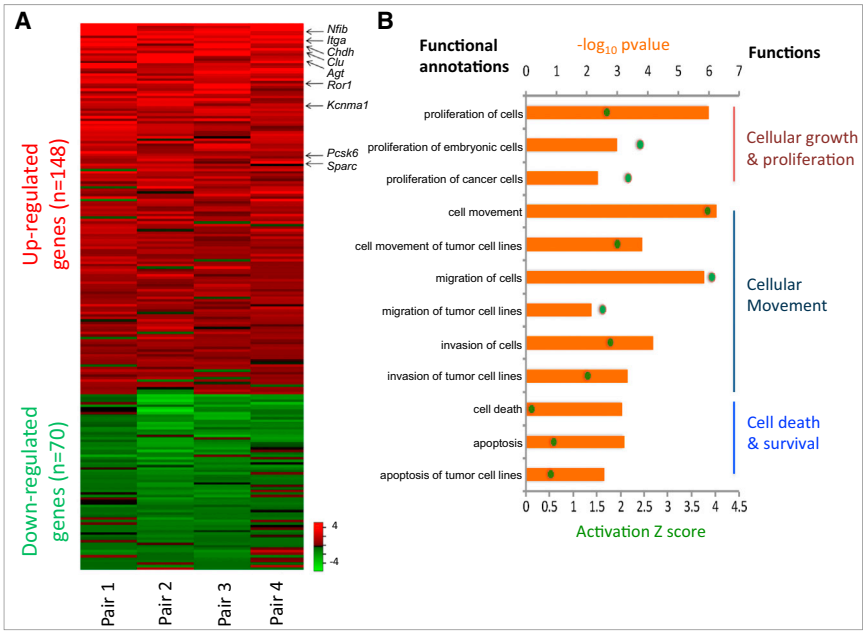

Figure 4. Key Changes in Cancer Progression Following NFIB Overexpression In Vitro

(A) Analysis of the gene expression changes following *Nfib* overexpression in four mouse SCLC primary cell lines (heatmap). DEGs were selected if expressed in at least three out of four samples. Values are represented as log2 fold change. Red, upregulated (average log2 fold change > 0.5); green, downregulated genes (average log2 fold change < −0.5).

(B) Ingenuity pathway analysis (IPA) of differentially expressed genes based on *Z* score and p value. The biological functions that are expected to be increased according to the gene expression changes in our dataset were identified using the IPA regulation *Z* score algorithm (green dot). The p value was calculated with the Fischer's exact test (p value ≤ 0.05).

(C) Genes involved in cell movement. Orange dashed line, predicting activation of cell movement; green dashed line, unknown directionality; black dashed line, effect not predicted.

(D) Validation of several genes in (C) by qPCR. Error bars represent mean ± SD.

See also Figure S5 and Table S1.

of 148 upregulated genes were implicated in cell motility, and 50 out of 148 upregulated genes were associated with cell death and survival (Figure 4B). The cell motility category showed the highest activation *Z* score of 3.83, strongly indicating that genes upregulated following NFIB overexpression increased cell motility (Figure 4C). Some of the upregulated genes that were assigned to cell movement, cell death, and survival were validated by qPCR (Figure 4D; Figure S5D).

NFIB Drives Tumor Dedifferentiation and Invasion

The ability to metastasize is often associated with dedifferentiation (Ellenbroek et al., 2012). Given the strong metastatic behavior of NFIB expressing tumors, we asked whether NFIB was associated with dedifferentiation. Indeed, early lesions that were low or negative for NFIB expressed high levels of SYN, whereas lesions with strong NFIB expression showed a clear reduction in SYN (Figures 5A and 5B). Similarly, in advanced lesions, the NFIB high (NFIB^{hi}) populations showed signs of dedifferentiation, as judged by a decreased level of SYN (Figures 5D, 5E, S6A, and S6B).

Another well-known prometastatic feature is increased invasiveness and decreased expression of adhesion molecules, such as E-cadherin (CDH1). All early lesions expressed CDH1, regardless of the NFIB level (Figures 5C and S6C), whereas NFIB^{hi} "dedifferentiated" populations within advanced lesions had frequently lost this marker (Figure 5F).

Based on the above, we predicted an increase in both dedifferentiation and invasiveness within the Nfib cohort as compared to control and Mycl cohorts. Indeed, a large proportion of the tumors in the lungs of control and Mycl mice expressed high levels of CGRP and CDH1 and showed limited invasion (Figures 5G and 5K; data not shown). Still, we often found areas negative for CDH1 (CDH1^{-}) juxtaposed to CDH1^{hi} areas (Figures 5G, 5H, and S6D), the former possibly resulting from reseeding events. The CDH1^{-} cells expressed high levels of NFIB and were CGRP/SYN^{lo} (Figures 5I, S6E, and S6F). These NFIB^{hi}/CGRP^{lo}/CDH1^{-} sub-populations often presented as pools of dedifferentiated tumor cells that invaded perivascular and peribronchial spaces, forming sheath-like patterns that are indicative of their strong disseminating capability (Figures 5H, 5I, and 5L). Consistent with this, tumors in the Nfib cohort were predominantly invasive and consisted primarily of NFIB^{hi}/CGRP^{lo}/CDH1^{-} cells (Figure 5J). Interestingly, while

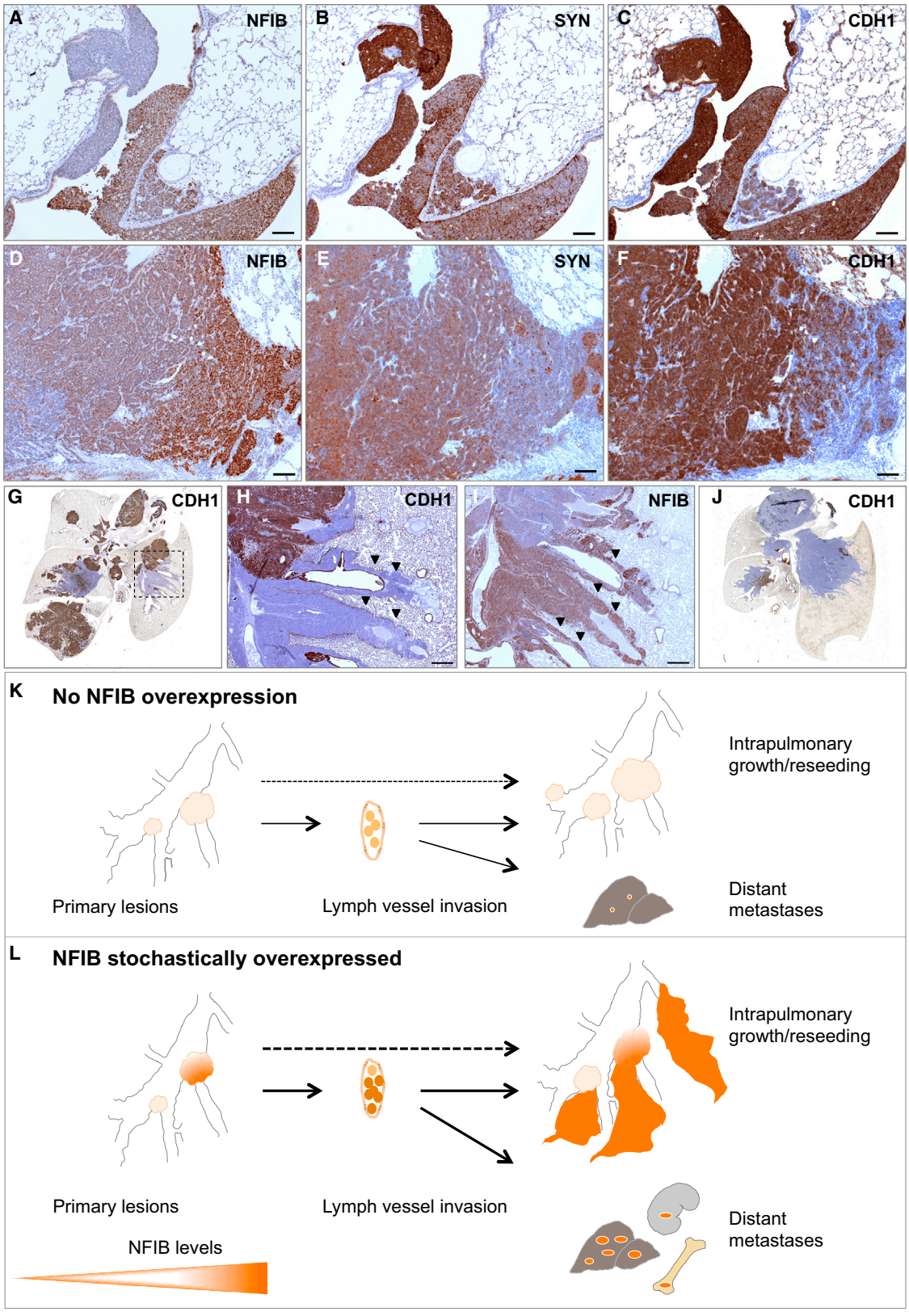

(legend on next page)

we often found scattered p44/42 MAPK-positive cells within NFIB^{lo}/CGRP^{hi}/CDH1^{hi} regions, the NFIB^{hi}/CGRP^{lo}/CDH1^{-} areas were invariably p44/42-negative (Figures S6G–S6I).

All tumors, irrespective of NFIB levels, expressed ASCL1, a factor required for SCLC survival, and SOX2, shown to be amplified in a subset of SCLCs (Augustyn et al., 2014; Rudin et al., 2012). TTF1, also often expressed in SCLC (Travis, 2012), showed variable levels without a clear correlation with NFIB staining (data not shown).

Lungs from animals in all cohorts contained frequent vascular invasions that were already present early on following tumor induction (Figure S7A). To define invasion routes, we stained sequential lung sections with SYN, CD31, and podoplanin to mark NE cells, blood, and lymph vessels. NE cells were found in clusters and invaded mainly lymph vessels (Figures S7B and S7C; data not shown). Both CDH1^{+} and CDH1^{-} cells could be found within vessels (Figure S7D). NFIB levels were moderate to high in NE cells present in lymph vessels (Figures S7E and S7F) and correlated with a stronger lymphovascular invasion (LVI) phenotype.

Given the abundant LVIs in our mouse model we were curious to see whether the LVIs previously reported for human SCLC show prominent expression of NFIB. Histological sections of SCLC from patients in which this could be assessed are not readily available. However, we did obtain sections from a human large cell neuroendocrine carcinoma (LCNEC) that showed LVIs (Figure S7G). Consistent with the mouse data, NE cells in these sections were NFIB^{hi} (Figure S7H) while being CDH^{-} (Figure S7I). This suggests that the process of tumor progression in high-grade NE tumors may also be linked to NFIB expression in humans. Indeed, critical driver lesions (RB1, p53, MYC, and NFIB) and changes in the expression of differentiation markers (CDH1, CGRP, SYN) as well as the route of tumor dissemination (LVI) are shared features of SCLC in humans and mice (Figures 5K and 5L).

NFIB Expression Is Correlated with Metastatic Disease in Human SCLC and LCNEC

The phenotypes described above point to the importance of NFIB in the acquisition of a high-grade invasive, dedifferentiated, and metastatic tumor state. We therefore tested whether NFIB is expressed in pulmonary neuroendocrine tumors (pNETs) of various grades. According to the recent edition of the World Health Organization, pNETs are classified into low-grade typical carcinoids (TCs), intermediate grade atypical carcinoid (AC), and high-grade NE carcinomas, the latter including both (LCNEC and SCLC) (Travis et al., 2015). We retrieved a panel of 48 pNET tumor samples from the archive of the Antoni van Leeuwenhoek hospital. The panel included TC, AC, LCNEC, and SCLC cases. Strikingly, while being absent or weakly expressed in all TC (10) (Figures 6A, 6B, and 6M) and in all AC (6) samples (Figures 6D, 6E, and 6M), NFIB was highly expressed in 22 out of 26 SCLC samples, including those derived from primary (13 out of 15) and metastatic (9 out of 11) sites (Figures 6J, 6K, and 6M). A significant spread in NFIB expression was evident in LCNEC cases (high expression in three out of six cases) (Figures 6G, 6H, and 6M). CDH1 expression showed an opposite trend, with rather high expression in more differentiated, low- and intermediate-grade TC and AC, and significantly lower average expression in SCLC and LCNEC (Figures 6C, 6F, 6I, 6L, and 6N). Strikingly, NFIB^{lo} expressing cases showed significantly better overall survival compared to NFIB^{hi} cases (Figure 6O). Further analysis of patient data indicated that five out of seven NFIB^{lo} cases represented low-stage SCLC and LCNEC (stage I/II), and none of the NFIB^{lo} category presented with stage IV disease characterized by distant metastases. In contrast, 23 out of 24 patients in the NFIB^{hi} group for which we had records had stage III/IV disease. These data fully align with the results obtained in our mouse models.

DISCUSSION

Well-designed mouse models are invaluable for understanding the processes underlying initiation, progression, and metastatic spread of SCLC and to rationally design better intervention strategies (Semenova et al., 2015). This is particularly important in view of the poor access to both early and progressed tumor lesions in patients. Several groups have successfully utilized *Rb1*$^{F/F}$;*Trp53*$^{F/F}$ mouse models to identify and validate other oncogenic drivers, including MYCL, PTEN, and RBL2 as well as NOTCH and Hedgehog pathway components (Gazdar et al., 2015). Genome sequencing of human SCLC has pointed to a number of additional drivers that likely lead to the variations we observe in NE tumors. Here we show that NFIB is a prominent driver in SCLC, with a key role in shaping the aggressive nature of this tumor type.

NFIB Accelerates SCLC Initiation

We show that NFIB significantly accelerates SCLC initiation and progression in our mouse models. Forced NFIB overexpression allowed for more efficient and frequent initiation of NE lesions and led to tumor development at new sites, i.e., trachea. The striking predominance of tracheal lesions in the Nfib/Mycl cohort (with several cases in the Nfib cohort) and its absence in the Mycl cohort supports the critical role of NFIB in the development of these tumors. We hypothesize that the combination of the

Figure 5. NFIB Drives Tumor Dedifferentiation and Invasion

(A–C) Early lesions NFIB (A), SYN (B), and CDH1 (C) staining, respectively (Nfib cohort).

(D–F) Advanced lesion NFIB (D), SYN (E), and CDH1 (F) staining, respectively (Mycl cohort).

(G) Whole lung, CDH1 staining (Mycl cohort).

(H and I) Part of the lung indicated with dotted area in (G), CDH1 (H) and NFIB (I), respectively. Invasive sheaths indicated with arrowheads.

(J) Whole lung, CDH1 staining (Nfib cohort).

(K and L) Diagrams of tumor growth and local and distant metastatic dissemination. NE tumor cells are abundantly found in lymph vessels. Without NFIB overexpression, intrapulmonary dissemination and metastatic load in liver is very limited (K). With NFIB overexpression, there is massive intrapulmonary dissemination, large metastatic load in the liver, and metastasis to kidney and bone (L).

Scale bars in (A)–(F) represent 100 μm. Scale bars in (H) and (I) represent 500 μm. See also Figure S6.

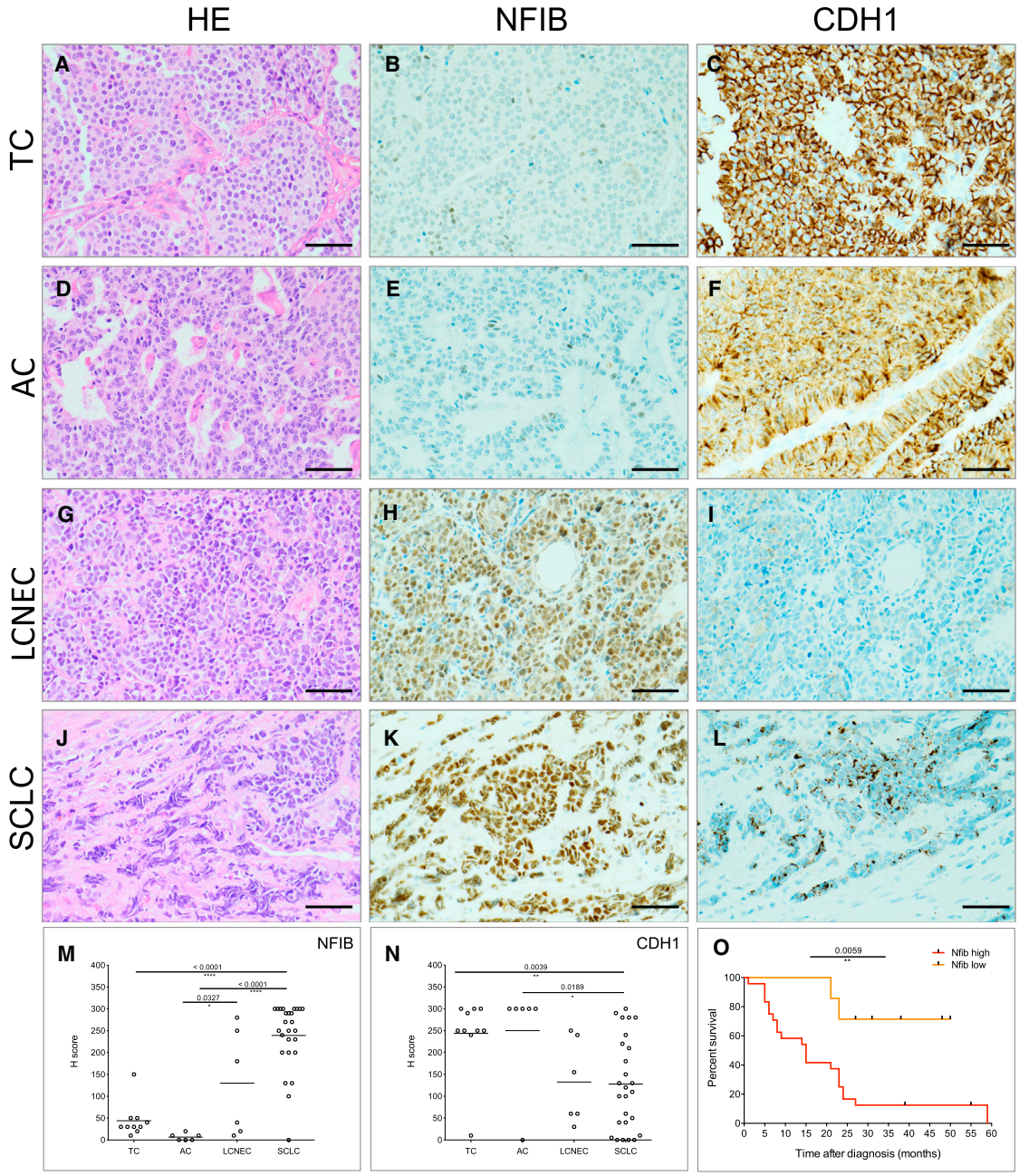

Figure 6. NFIB Marks Metastatic Disease in Patients

(A–C) Representative image of H&E (A), NFIB (B), and CDH1 (C) expression in typical carcinoid (TC).

(D–F) Representative image of H&E (D), NFIB (E), and CDH1 (F) expression in atypical carcinoid (AC).

(G–I) Representative image of H&E (G), NFIB (H), and CDH1 (I) expression in large cell NE carcinoma (LCNEC).

(J–L) Representative image of H&E (J), NFIB (K), and CDH1 (L) expression in SCLC.

(M and N) Quantification of NFIB (M) and CDH1(N) expression in human pNET samples, respectively.

(O) Survival curves of patients within high-grade pNET (LCNEC and SCLC).

See also Figure S7 and Table S2.

single-cell nature of NE cells in the trachea and environmental factors make these cells more refractory to tumor initiation and that NFIB is required to overcome these less favorable conditions for outgrowth.

NFIB Overexpression Is Associated with Increased Chromosomal Instability

An unexpected observation was the increased chromosomal instability in NFIB-driven tumors. Gene expression analysis did

not reveal a candidate gene or signature associated with the control of cell replication or DNA repair. However, the increase in chromosomal aberrations observed in NFIB overexpressing cells may well be explained by a higher tolerance for chromosomal instability resulting from NFIB's anti-apoptotic activity as previously found in SCLC cell lines and mouse embryonic fibroblasts (Dooley et al., 2011).

NFIB Is a Potent Driver of Metastasis

We show that NFIB promotes metastasis not only by increasing the local dissemination of the tumor cells within the lung but also by altering their metastatic profile, permitting colonization of a wider set of tissues. We identified gene signatures for proliferation and cellular movement imposed by NFIB overexpression in mouse SCLC cell lines. The profiles were in line with the observed phenotypes in the NFIB driven tumors and highlighted the ability of NFIB to modify a number of distinct behavioral features of NE cells, making them more capable to invade and colonize foreign sites.

We have previously shown that communication between NE (p44/42-negative) and NonNE (p44/42-positive) cells is required for efficient metastasis of subcutaneously grafted SCLC cells (Calbo et al., 2011; Kwon et al., 2015). Interestingly, p44/22-positive cells were only found in NFIB^{lo} regions. Although NonNE cell cultures can be easily established from isolated tumors, their identity in vivo remains elusive. It might be that these p44/42-positive cells represent this NonNE population and that they play their own specific role in assisting NE cell survival, outgrowth, and dissemination.

NFIB Overexpression Results in Dedifferentiated Aggressive Tumors

Tumors in our SCLC mouse models showed both differentiated and dedifferentiated characteristics. High NFIB expression was associated with dedifferentiation and invasive behavior evidenced by the presence of perivascular and peribronchial sheath-like dissemination. This type of invasive behavior was most prevalent in the Nfib cohort. In line with this, we found a consistent negative correlation between the expression of NFIB and NE differentiation markers in advanced lesions. Unlike advanced lesions, a subset of NFIB^{hi} early lesions showed high levels of NE differentiation markers, indicating that NFIB-driven dedifferentiation is at least in part a gradual process.

Once tumors start to progress, we see striking heterogeneity with respect to CDH1 expression, loss of which has been associated with metastatic spread (Schneider and Kolligs, 2015; Singhai et al., 2011). All early lesions are CDH1^{+}, in LVIs the expression is heterogeneous, and it is lost in disseminated tumors. Consequently, the CDH1^{-} lesions might well have arisen from reseeding events. The pattern of colonization within the lung supports this. In conclusion, NFIB is critical for forcing dedifferentiation of NE tumor lesions, thereby augmenting their invasive behavior.

NFIB Regulation

NFIB belongs to a family of transcription factors capable of binding and regulating a plethora of targets. This makes the dissection of the exact molecular mechanisms underlying NFIB-mediated oncogenic transformation a challenge. At the same time, this multifaceted function might be needed for progression and colonization of new metastatic sites.

In contrast to the highly conserved N-terminal DNA binding domain, the C-terminal region of NFIB diverges extensively between members of the NFI transcription factor family as well as between isoforms (Liu et al., 1997). The C-terminal region encodes a putative transactivation domain (Mermod et al., 1989). Overexpression of the two isoforms that differ in this C-terminal region resulted in indistinguishable phenotypes. Therefore, the role of this domain for tumor progression and metastasis appears to be negligible.

Little is known about the regulation of NFIB expression. The transcription factor PAX6, a member of the paired box gene family, has been shown to bind and regulate NFI family proteins, including NFIB (Holm et al., 2007; Ninkovic et al., 2013). In addition, several microRNAs (mRNAs), such as miR-124, miR-1246, and miR-153, have been reported to regulate NFIB (Tsai et al., 2014; Wang et al., 2015; Zhang et al., 2015). These miRNAs bind NFIB transcripts in the 3′ UTR. Altered expression of these miRNAs could therefore lead to NFIB upregulation in tumors.

It is worth noting that the mouse model brought NFIB to light, which otherwise would have been overlooked due to paucity of genomic aberrations encompassing the NFIB locus in human SCLC. This also emphasizes the added value of monitoring RNA and protein expression in parallel with the identification of genomic aberrations. The importance of conducting such analyses at the single cell level is nicely illustrated by the extensive and profound heterogeneity that we observe in mouse SCLC and that is also seen in human SCLC.

NFIB Marks Metastatic Disease in Human SCLC and LCNEC

The important role of NFIB in mouse SCLC prompted us to scrutinize its relevance for SCLC development in human. Utilizing a panel of human pNETs, we could show that NFIB is often highly expressed in NE human tumors, such as SCLC and LCNEC, as compared to the low- and intermediate-grade cancers, such as TC and AC.

Importantly, the majority of high-stage SCLC and LCNEC were NFIB^{hi}, whereas the few tumor samples that were NFIB^{lo} represented mainly stage I/II cases, and consequently these patients showed prolonged survival. This points to the biological significance of NFIB in commanding a highly proliferative, dedifferentiated, migratory, and invasive state that is a characteristic of metastatic disease in patients. The data are highly consistent with our results obtained in the mouse. When patients present with stage I/II disease, high expression of NFIB may already be indicative for a high probability of early progression with micro-metastasis. Therefore, our data point to a possible prognostic value of NFIB and call for analysis of a large patient cohort. However, before such prognostic marker can be useful, efficient early detection methods (i.e., liquid biopsy sequencing) have to be in place.

In summary, high NFIB expression marks high-grade tumor populations both in a mouse model of SCLC and in human pNETs. The specific set of features influenced by NFIB makes this transcription factor particularly potent in promoting tumor progression and metastatic dissemination. Therefore, analysis

of targets downstream of NFIB and detailed dissection of molecular mechanisms involved in NFIB driven phenotypes may help to understand the key biological peculiarities of SCLC. In the same vein it will be important to identify the gene(s) that control the levels of NFIB as they likely serve as important master regulators of metastasis.

EXPERIMENTAL PROCEDURES

More detailed procedures are described in the Supplemental Information.

Ethics Statement

The study was performed in accordance with the Dutch and European regulations on care and protection of laboratory animals. All animal experiments were approved by the local animal experimental committee, DEC NKI (OZP ID: 10023).

Genetic Engineering in *Rb1*$^{F/F}$*;Trp53*$^{F/F}$ ESCs and Generation of Mice

The *pFrt-invCAG-Nfib_v1-Luc* and *pFrt-invCAG-Nfib_v3-Luc* vectors were introduced in a rederived *Col1a1-frt* targeted *Rb1*$^{F/F}$*;Trp53*$^{F/F}$ embryonic stem cell (ESC) clone (NKI GEMM-ESC resource at www.infrafrontier.eu, clone TMA11101) by means of Flpe-mediated transgene integration as described (Huijbers et al., 2015).

DNA Sequencing and Copy-Number Profiling

Genomic DNA library was prepared by TruSeq DNA LT Sample Preparation kit (Illumina) and was sequenced using an Illumina HiSeq2000/2500 machine according to manufacturer's instructions. To obtain copy-number profiles, we used CopywriteR tool (Kuilman et al., 2015).

Next-generation MPS mate-pair libraries were prepared using the Nextera Mate Pair Sample Preparation Kit (Illumina) (Stephens et al., 2011).

Human SCLC Patient Specimens

This study was approved by the institutional review board of the NKI-AVL. We collected archived formalin fixed and paraffin embedded samples of 48 TC, AC, LCNEC, and SCLC patients. The samples were primary and metastatic tumors diagnosed as stage I/IV. The H-score was determined by assessing the extent of immunoreactivity for NFIB and CDH1 (ECAD) by K.M. and E.A.S. (Table S2). An H-score above 150 was considered NFIB^{hi}. Overall survival was determined by the length of time from diagnosis to last date of follow-up at which patients were still alive.

Statistical Analysis

Kaplan-Meier survival curves were analyzed using the log-rank test. All p values were calculated using a nonparametric Mann-Whitney test. Data shown in column graphs represent the mean ± SD. Statistical analyses were performed by GraphPad Prism6.

ACCESSION NUMBERS

The accession number for the sequences reported in this paper is NCBI BioProject: SRP075877. The accession number for RNA sequencing data is GEO: GSE82005.

SUPPLEMENTAL INFORMATION

Supplemental Information includes Supplemental Experimental Procedures, seven figures, and two tables and can be found with this article online at http://dx.doi.org/10.1016/j.celrep.2016.06.020.

AUTHOR CONTRIBUTIONS

E.A.S, M.-C.K., E.v.M., I.J.H., and A.B. conceived, designed, and analyzed the mouse experiments. M.C., J.v.d.V., J.-P.L., and N.P. performed these experiments. C.P. and I.J.H. conceived, designed, and made the mouse models. E.A.S., K.M., and E.F.S. conceived, designed, and analyzed human experiments. K.M., D.P., and W.A.B. performed these experiments. E.A.S. and J.-Y.S. performed the histopathological survey of mouse tissues. J.Z. performed the stainings. R.B., O.K., T.K., and A.V. performed computational analysis. E.A.S, M.-C.K., I.J.H., and A.B. wrote the manuscript with input from K.M., J.-Y.S., and R.B.

ACKNOWLEDGMENTS

We thank members of the animal facility of the Netherlands Cancer Institute for maintaining the mice; the division of animal pathology members Ellen Riem, Joost van Ooij, Lex de Vrije, and Jelrik van der Meer for producing high-quality histopathologic samples; and the sequencing facility for sequencing the numerous samples. We thank Rahmen Bin Ali and Fina van der Ahé for excellent technical assistance. We thank Patrick Min for assistance with image preparation. We would like to acknowledge the NKI-AVL Core Facility Molecular Pathology & Biobanking (CFMPB) for supplying NKI-AVL Biobank material and/or lab support. This study was supported by a WKO grant to A.B. by the Dutch Cancer Society, a Synergy ERC grant in which A.B. is one of the principal investigators, and a National Roadmap grant for Large-Scale Research Facilities of the Netherlands Organization for Scientific Research.

Received: March 31, 2016
Revised: May 24, 2016
Accepted: June 1, 2016
Published: June 30, 2016

REFERENCES

Andreasen, S., Persson, M., Kiss, K., Homøe, P., Heegaard, S., and Stenman, G. (2016). Genomic profiling of a combined large cell neuroendocrine carcinoma of the submandibular gland. Oncol. Rep. *35*, 2177–2182.

Augustyn, A., Borromeo, M., Wang, T., Fujimoto, J., Shao, C., Dospoy, P.D., Lee, V., Tan, C., Sullivan, J.P., Larsen, J.E., et al. (2014). ASCL1 is a lineage oncogene providing therapeutic targets for high-grade neuroendocrine lung cancers. Proc. Natl. Acad. Sci. USA *111*, 14788–14793.

Byers, L.A., and Rudin, C.M. (2015). Small cell lung cancer: where do we go from here? Cancer *121*, 664–672.

Calbo, J., van Montfort, E., Proost, N., van Drunen, E., Beverloo, H.B., Meuwissen, R., and Berns, A. (2011). A functional role for tumor cell heterogeneity in a mouse model of small cell lung cancer. Cancer Cell *19*, 244–256.

Cermáková, K., Tesina, P., Demeulemeester, J., El Ashkar, S., Méreau, H., Schwaller, J., Rezáčová, P., Veverka, V., and De Rijck, J. (2014). Validation and structural characterization of the LEDGF/p75-MLL interface as a new target for the treatment of MLL-dependent leukemia. Cancer Res. *74*, 5139–5151.

Chang, C.Y., Pasolli, H.A., Giannopoulou, E.G., Guasch, G., Gronostajski, R.M., Elemento, O., and Fuchs, E. (2013). NFIB is a governor of epithelial-melanocyte stem cell behaviour in a shared niche. Nature *495*, 98–102.

Dooley, A.L., Winslow, M.M., Chiang, D.Y., Banerji, S., Stransky, N., Dayton, T.L., Snyder, E.L., Senna, S., Whittaker, C.A., Bronson, R.T., et al. (2011). Nuclear factor I/B is an oncogene in small cell lung cancer. Genes Dev. *25*, 1470–1475.

Ellenbroek, S.I., Iden, S., and Collard, J.G. (2012). Cell polarity proteins and cancer. Semin. Cancer Biol. *22*, 208–215.

French, J.D., Johnatty, S.E., Lu, Y., Beesley, J., Gao, B., Kalimutho, M., Henderson, M.J., Russell, A.J., Kar, S., Chen, X., et al.; On Behalf Of The Ovarian Cancer Association Consortium; Australian Ovarian Cancer Study Group; Australian Ovarian Cancer Study (2016). Germline polymorphisms in an enhancer of PSIP1 are associated with progression-free survival in epithelial ovarian cancer. Oncotarget *7*, 6353–6368.

Gazdar, A.F., Savage, T.K., Johnson, J.E., Berns, A., Sage, J., Linnoila, R.I., MacPherson, D., McFadden, D.G., Farago, A., Jacks, T., et al. (2015). The

comparative pathology of genetically engineered mouse models for neuroendocrine carcinomas of the lung. J. Thorac. Oncol. *10*, 553–564.

George, J., Lim, J.S., Jang, S.J., Cun, Y., Ozretić, L., Kong, G., Leenders, F., Lu, X., Fernández-Cuesta, L., Bosco, G., et al. (2015). Comprehensive genomic profiles of small cell lung cancer. Nature *524*, 47–53.

Ghanem, G., and Fabrice, J. (2011). Tyrosinase related protein 1 (TYRP1/gp75) in human cutaneous melanoma. Mol. Oncol. *5*, 150–155.

Gronostajski, R.M. (2000). Roles of the NFI/CTF gene family in transcription and development. Gene *249*, 31–45.

Han, W., Jung, E.M., Cho, J., Lee, J.W., Hwang, K.T., Yang, S.J., Kang, J.J., Bae, J.Y., Jeon, Y.K., Park, I.A., et al. (2008). DNA copy number alterations and expression of relevant genes in triple-negative breast cancer. Genes Chromosomes Cancer *47*, 490–499.

Harris, L., Genovesi, L.A., Gronostajski, R.M., Wainwright, B.J., and Piper, M. (2015). Nuclear factor one transcription factors: divergent functions in developmental versus adult stem cell populations. Dev. Dyn. *244*, 227–238.

Holm, P.C., Mader, M.T., Haubst, N., Wizenmann, A., Sigvardsson, M., and Götz, M. (2007). Loss- and gain-of-function analyses reveal targets of Pax6 in the developing mouse telencephalon. Mol. Cell. Neurosci. *34*, 99–119.

Hsu, Y.C., Osinski, J., Campbell, C.E., Litwack, E.D., Wang, D., Liu, S., Bachurski, C.J., and Gronostajski, R.M. (2011). Mesenchymal nuclear factor I B regulates cell proliferation and epithelial differentiation during lung maturation. Dev. Biol. *354*, 242–252.

Huijbers, I.J., Bin Ali, R., Pritchard, C., Cozijnsen, M., Kwon, M.C., Proost, N., Song, J.Y., de Vries, H., Badhai, J., Sutherland, K., et al. (2014). Rapid target gene validation in complex cancer mouse models using re-derived embryonic stem cells. EMBO Mol. Med. *6*, 212–225.

Huijbers, I.J., Del Bravo, J., Bin Ali, R., Pritchard, C., Braumuller, T.M., van Miltenburg, M.H., Henneman, L., Michalak, E.M., Berns, A., and Jonkers, J. (2015). Using the GEMM-ESC strategy to study gene function in mouse models. Nat. Protoc. *10*, 1755–1785.

Iwakawa, R., Takenaka, M., Kohno, T., Shimada, Y., Totoki, Y., Shibata, T., Tsuta, K., Nishikawa, R., Noguchi, M., Sato-Otsubo, A., et al. (2013). Genome-wide identification of genes with amplification and/or fusion in small cell lung cancer. Genes Chromosomes Cancer *52*, 802–816.

Kuilman, T., Velds, A., Kemper, K., Ranzani, M., Bombardelli, L., Hoogstraat, M., Nevedomskaya, E., Xu, G., de Ruiter, J., Lolkema, M.P., et al. (2015). CopywriteR: DNA copy number detection from off-target sequence data. Genome Biol. *16*, 49.

Kwon, M.C., and Berns, A. (2013). Mouse models for lung cancer. Mol. Oncol. *7*, 165–177.

Kwon, M.C., Proost, N., Song, J.Y., Sutherland, K.D., Zevenhoven, J., and Berns, A. (2015). Paracrine signaling between tumor subclones of mouse SCLC: a critical role of ETS transcription factor Pea3 in facilitating metastasis. Genes Dev. *29*, 1587–1592.

Liu, Y., Bernard, H.U., and Apt, D. (1997). NFI-B3, a novel transcriptional repressor of the nuclear factor I family, is generated by alternative RNA processing. J. Biol. Chem. *272*, 10739–10745.

McFadden, D.G., Papagiannakopoulos, T., Taylor-Weiner, A., Stewart, C., Carter, S.L., Cibulskis, K., Bhutkar, A., McKenna, A., Dooley, A., Vernon, A., et al. (2014). Genetic and clonal dissection of murine small cell lung carcinoma progression by genome sequencing. Cell *156*, 1298–1311.

Mermod, N., O'Neill, E.A., Kelly, T.J., and Tjian, R. (1989). The proline-rich transcriptional activator of CTF/NF-I is distinct from the replication and DNA binding domain. Cell *58*, 741–753.

Meuwissen, R., Linn, S.C., Linnoila, R.I., Zevenhoven, J., Mooi, W.J., and Berns, A. (2003). Induction of small cell lung cancer by somatic inactivation of both Trp53 and Rb1 in a conditional mouse model. Cancer Cell *4*, 181–189.

Mosakhani, N., Pazzaglia, L., Benassi, M.S., Borze, I., Quattrini, I., Picci, P., and Knuutila, S. (2013). MicroRNA expression profiles in metastatic and non-metastatic giant cell tumor of bone. Histol. Histopathol. *28*, 671–678.

Ninkovic, J., Steiner-Mezzadri, A., Jawerka, M., Akinci, U., Masserdotti, G., Petricca, S., Fischer, J., von Holst, A., Beckers, J., Lie, C.D., et al. (2013). The BAF complex interacts with Pax6 in adult neural progenitors to establish a neurogenic cross-regulatory transcriptional network. Cell Stem Cell *13*, 403–418.

Piper, M., Barry, G., Harvey, T.J., McLeay, R., Smith, A.G., Harris, L., Mason, S., Stringer, B.W., Day, B.W., Wray, N.R., et al. (2014). NFIB-mediated repression of the epigenetic factor Ezh2 regulates cortical development. J. Neurosci. *34*, 2921–2930.

Quattrini, I., Pollino, S., Pazzaglia, L., Conti, A., Novello, C., Ferrari, C., Pignotti, E., Picci, P., and Benassi, M.S. (2015). Prognostic role of nuclear factor/IB and bone remodeling proteins in metastatic giant cell tumor of bone: a retrospective study. J. Orthop. Res. *33*, 1205–1211.

Rudin, C.M., Durinck, S., Stawiski, E.W., Poirier, J.T., Modrusan, Z., Shames, D.S., Bergbower, E.A., Guan, Y., Shin, J., Guillory, J., et al. (2012). Comprehensive genomic analysis identifies SOX2 as a frequently amplified gene in small-cell lung cancer. Nat. Genet. *44*, 1111–1116.

Schneider, M.R., and Kolligs, F.T. (2015). E-cadherin's role in development, tissue homeostasis and disease: insights from mouse models: tissue-specific inactivation of the adhesion protein E-cadherin in mice reveals its functions in health and disease. BioEssays *37*, 294–304.

Semenova, E.A., Nagel, R., and Berns, A. (2015). Origins, genetic landscape, and emerging therapies of small cell lung cancer. Genes Dev. *29*, 1447–1462.

Singhai, R., Patil, V.W., Jaiswal, S.R., Patil, S.D., Tayade, M.B., and Patil, A.V. (2011). E-Cadherin as a diagnostic biomarker in breast cancer. N. Am. J. Med. Sci. *3*, 227–233.

Steele-Perkins, G., Plachez, C., Butz, K.G., Yang, G., Bachurski, C.J., Kinsman, S.L., Litwack, E.D., Richards, L.J., and Gronostajski, R.M. (2005). The transcription factor gene Nfib is essential for both lung maturation and brain development. Mol. Cell. Biol. *25*, 685–698.

Stephens, P.J., Greenman, C.D., Fu, B., Yang, F., Bignell, G.R., Mudie, L.J., Pleasance, E.D., Lau, K.W., Beare, D., Stebbings, L.A., et al. (2011). Massive genomic rearrangement acquired in a single catastrophic event during cancer development. Cell *144*, 27–40.

Travis, W.D. (2012). Update on small cell carcinoma and its differentiation from squamous cell carcinoma and other non-small cell carcinomas. Mod. Pathol. *25* (*Suppl 1*), S18–S30.

Travis, W.D., Brambilla, E., Nicholson, A.G., Yatabe, Y., Austin, J.H., Beasley, M.B., Chirieac, L.R., Dacic, S., Duhig, E., Flieder, D.B., et al. (2015). The 2015 World Health Organization classification of lung tumors: impact of genetic, clinical and radiologic advances since the 2004 classification. J. Thorac. Oncol. *10*, 1243–1260.

Tsai, P.C., Bake, S., Balaraman, S., Rawlings, J., Holgate, R.R., Dubois, D., and Miranda, R.C. (2014). MiR-153 targets the nuclear factor-1 family and protects against teratogenic effects of ethanol exposure in fetal neural stem cells. Biol. Open *3*, 741–758.

Wang, Y., Huang, C., Chintagari, N.R., Xi, D., Weng, T., and Liu, L. (2015). miR-124 regulates fetal pulmonary epithelial cell maturation. Am. J. Physiol. Lung Cell. Mol. Physiol. *309*, L400–L413.

Yang, Z.Q., Imoto, I., Pimkhaokham, A., Shimada, Y., Sasaki, K., Oka, M., and Inazawa, J. (2001). A novel amplicon at 9p23 - 24 in squamous cell carcinoma of the esophagus that lies proximal to GASC1 and harbors NFIB. Jpn. J. Cancer Res. *92*, 423–428.

Zhang, Q., Cao, L.Y., Cheng, S.J., Zhang, A.M., Jin, X.S., and Li, Y. (2015). p53-induced microRNA-1246 inhibits the cell growth of human hepatocellular carcinoma cells by targeting NFIB. Oncol. Rep. *33*, 1335–1341.

Cell Reports, Volume *16*

Supplemental Information

Transcription Factor NFIB Is a Driver of Small Cell Lung Cancer Progression in Mice and Marks Metastatic Disease in Patients

Ekaterina A. Semenova, Min-chul Kwon, Kim Monkhorst, Ji-Ying Song, Rajith Bhaskaran, Oscar Krijgsman, Thomas Kuilman, Dennis Peters, Wieneke A. Buikhuisen, Egbert F. Smit, Colin Pritchard, Miranda Cozijnsen, Jan van der Vliet, John Zevenhoven, Jan-Paul Lambooij, Natalie Proost, Erwin van Montfort, Arno Velds, Ivo J. Huijbers, and Anton Berns

Figure S1. Related to Figure 1. New mouse models for SCLC based on overexpression of two *Nfib* transcript variants

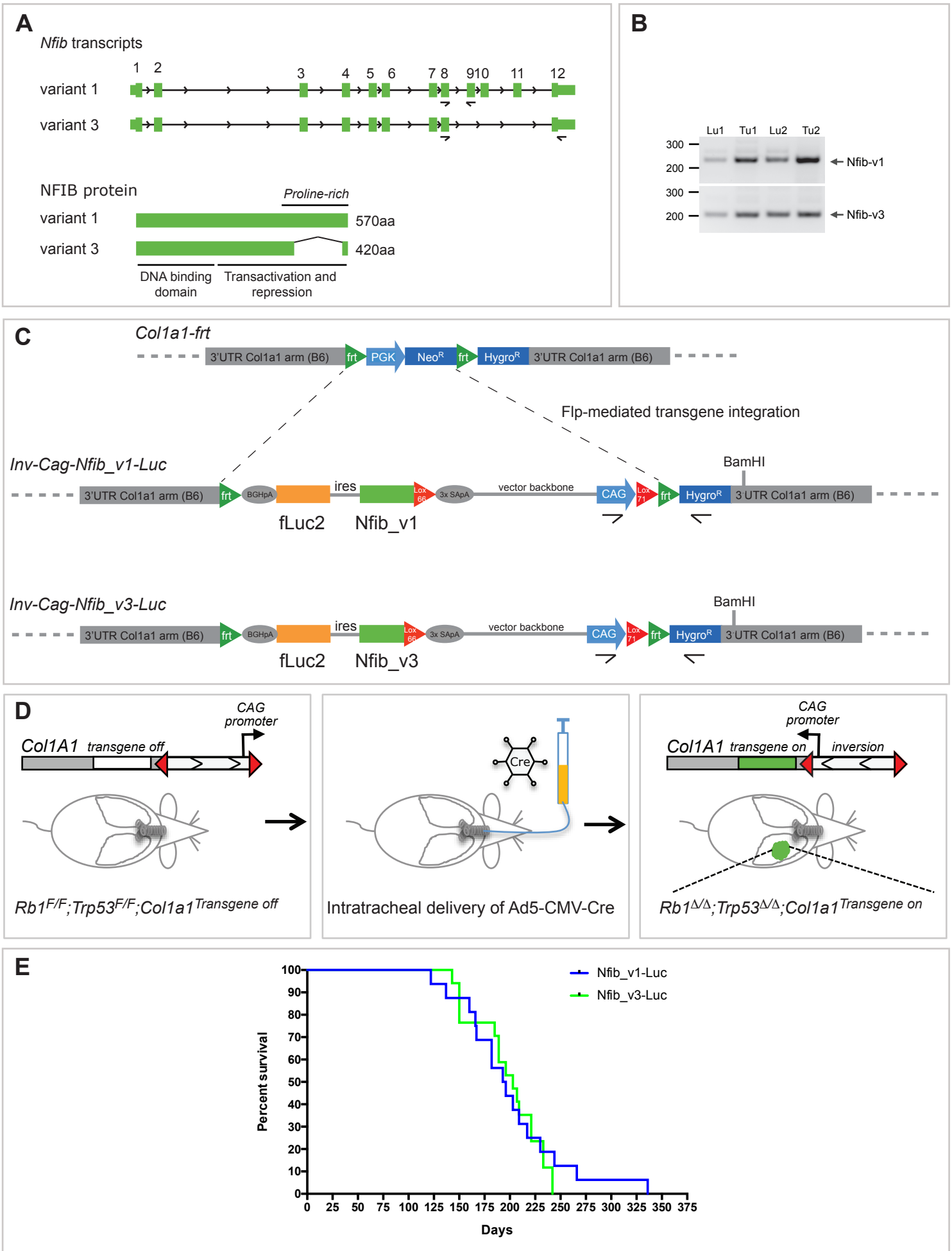

Figure S2. Related to Figure 1. Initial stages of tumor progression

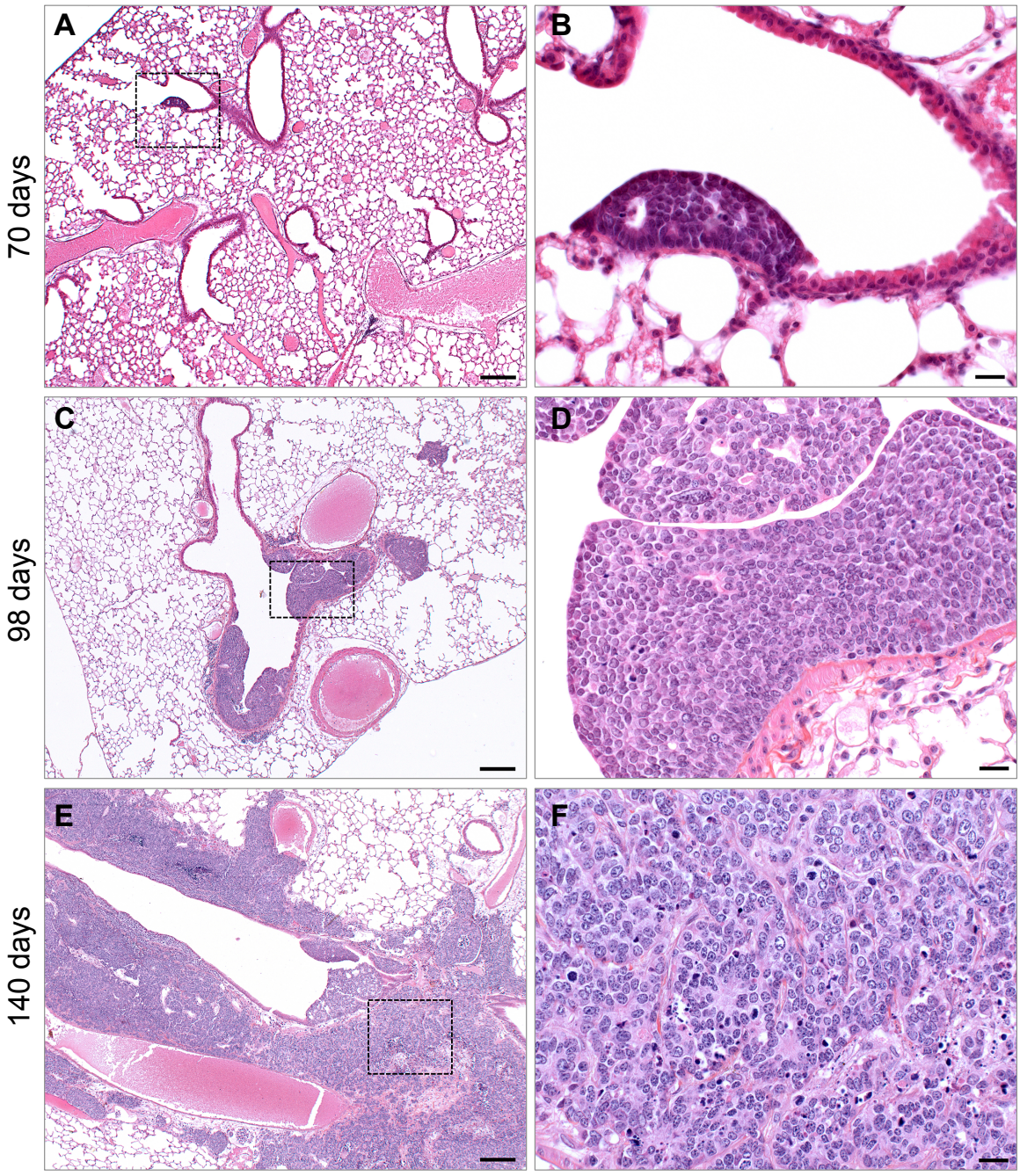

Figure S3. Related to Figure 1. Upper airway lesions in Nfib/Mycl cohort

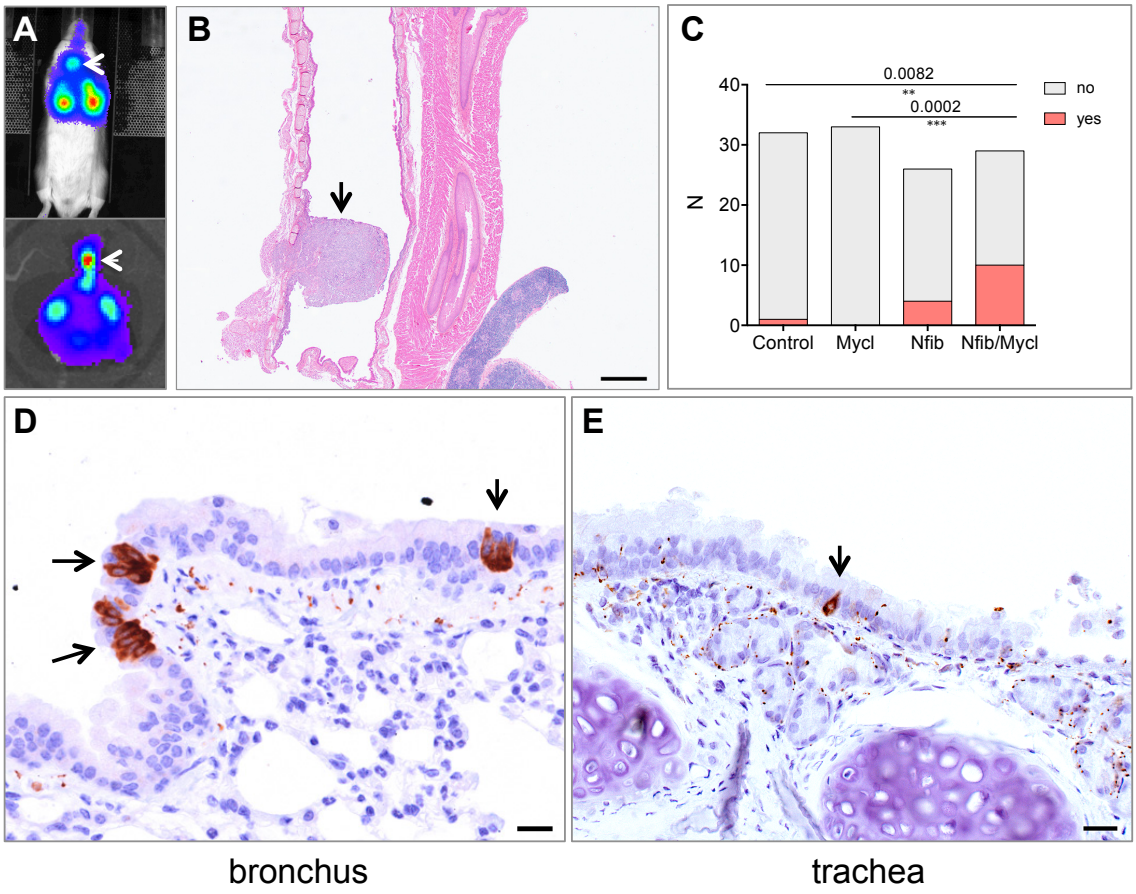

Figure S4. Related to Figure 3. NFIB promotes metastases and changes the metastatic profile

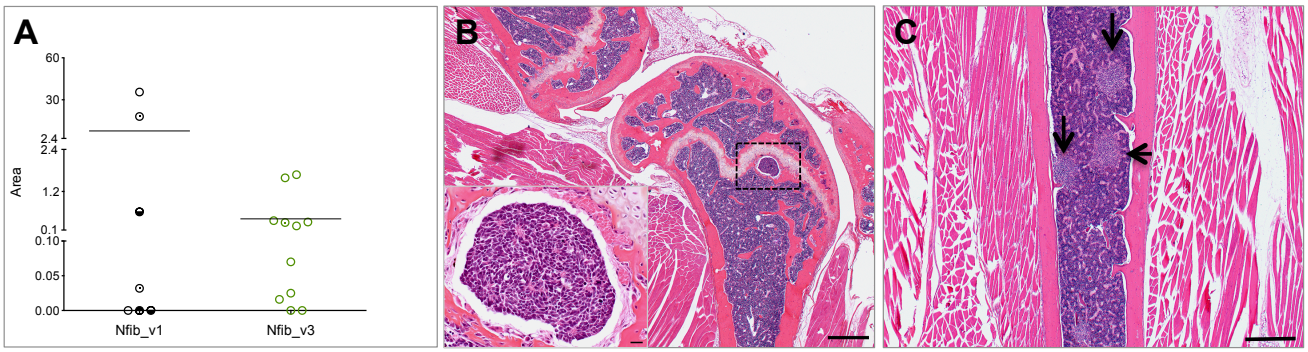

Figure S5. Related to Figure 4. Overexpression of mouse NFIB and the expression of putative NFIB target genes

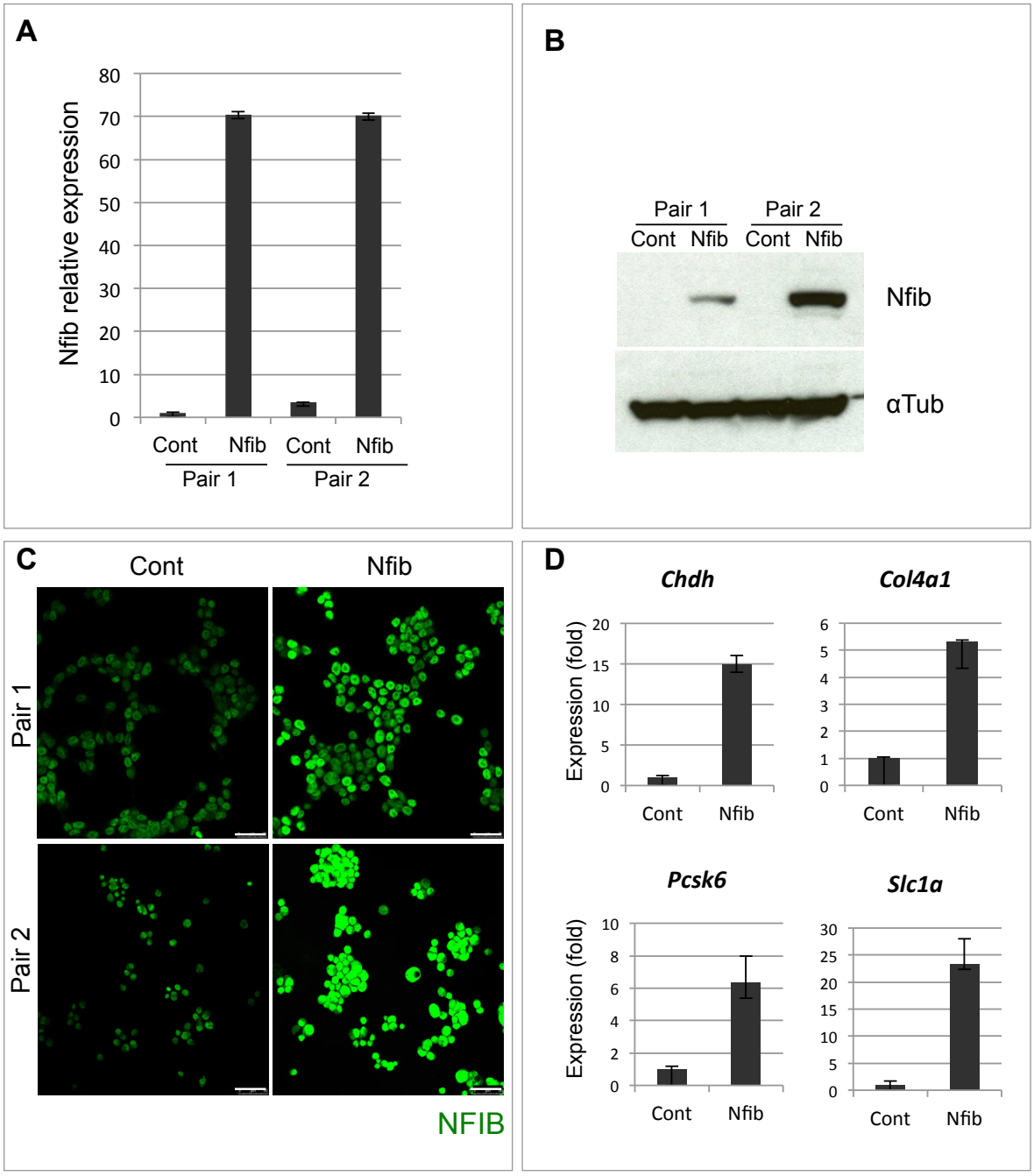

Figure S6. Related to Figure 5. NFIB drives tumor dedifferentiation and invasion

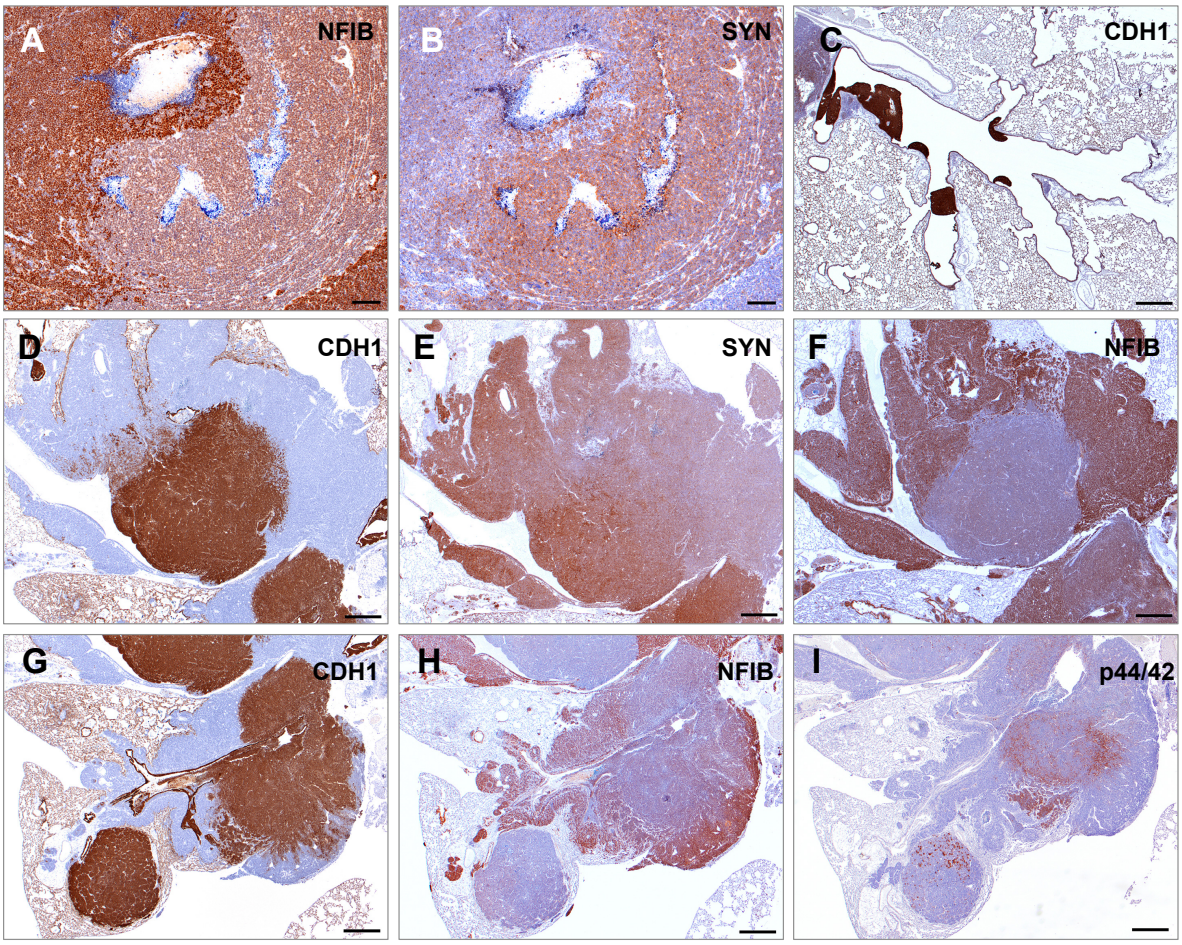

Figure S7. Related to Figure 5. NFIB drives tumor dedifferentiation and invasion (vascular invasion)

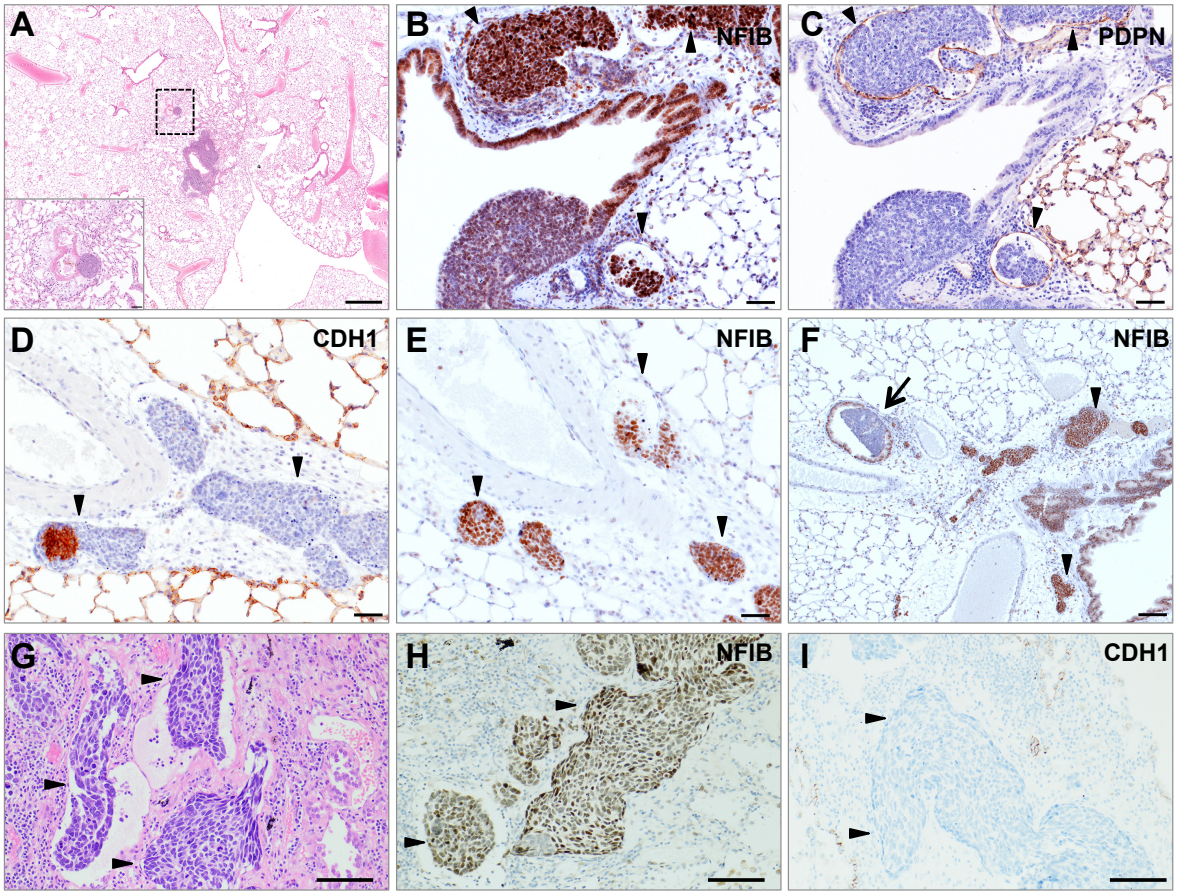

Figure S1. Related to Figure 1. New mouse models for SCLC based on overexpression of two *Nfib* transcript variants.
(A) Schematic representation of mouse *Nfib* transcripts and corresponding proteins. The Nfib protein from transcript variant 3 lacks the major part of a putative proline-rich transactivation domain at the C-terminus of the protein. Primers for RT-PCR analysis are indicated beneath exons 8, 9 and 12. (B) Detection of Nfib transcript variants 1 and 3 in normal mouse lung and in SCLC tumors for $Rb1^{F/F};Trp53^{F/F}$ mice with primers indicated in (A). Nfib_v1 gives a 234 bp product and Nfib_v3 a 210 bp. (C) Introduction of plasmids, *frt-invCag-Nfib_v1-Luc* or *frt-invCag-Nfib_v3-Luc*, in the *Col1a1-frt* construct in the *Col1a1* locus of the $Rb1^{F/F};Trp53^{F/F}$ embryonic stem cells (ESCs). ESCs were co-transfected with an *Nfib* coding inversion plasmid and a Flp-recombinase expression cassette. Clones were selected based on Hygromycin resistance. Correct Flp-mediated transgene integration was verified by a screening PCR with a forward primer in the CAG promoter and a reverse primer in the Hygromycin resistance gene. (D) Schematic representation of tumor induction. Mice with the $Rb1^{F/F};Trp53^{F/F};Col1a1^{Transgene}$ are intratracheally injected with an adeno-virus expressing Cre recombinase from the CMV promoter (Ad5-CMV-Cre). The virus infects lung epithelium, including neuro-endocrine cells. Cre recombinase deletes tumor suppressors *Rb1* and *Trp53*, and inverts the transgene between the two mutant loxP sites, i.e. Lox66-Lox71, leading to expression of the transgene, in this case the *Nfib* and the *Luciferase 2* gene. (E) Survival curve of two cohorts of Nfib mice, i.e. *InvCag-Nfib_v1-Luc;*$Rb1^{F/F};Trp53^{F/F}$ and *InvCag-Nfib_v3-Luc;*$Rb1^{F/F};Trp53^{F/F}$, following intratracheal injection with Ad5-CMV-Cre.

Figure S2. Related to Figure 1. Stages of tumor progression (Nfib/Mycl cohort)
(A) Representative HE of lung sections taken at 70 days following viral induction. (B) Magnification of the region in (A) indicated with the dotted line. (C) Representative HE of lung sections taken at 98 days following viral induction. (D) Magnification of the region in (C) indicated with the dotted line. (E) Representative HE of lung sections taken at 140 days following viral induction. (F) Magnification of the region in (E) indicated with the dotted line.
Scale bars in A, C, E represent 200 μm. Scale bars in B, D, F represent 20 μm.

Figure S3. Related to Figure 1. Upper airway lesions in Nfib/Mycl cohort
(A) Localized luciferase signal within the trachea (arrow). (B) Histological section of trachea with NE lesion (arrow). (C) Quantification of the number of animals with tracheal lesion within each cohort. (D) Section of bronchial epithelium of a normal lung (synaptophysin). (E) Section of the normal trachea (synaptophysin). Scale bar in B represents 500 μm. Scale bars in D and E represent 20 μm.

Figure S4. Related to Figure 3. NFIB promotes metastases and changes the metastatic profile. (A) Quantification of the percent area of liver samples covered by metastatic lesions in two transcript variant groups within Nfib cohort (Nfib_v1 and Nfib_v3). Circles with shaded upper half and shaded lower half indicate animals with kidney and bone metastasis, respectively. Circles marked with a central dot indicate animals with metastasis to both kidney and bone. (B and C) Metastasis within the bone and the bone marrow, respectively.

Figure S5. **Related to Figure 4. Overexpression of mouse NFIB and the expression of putative NFIB target genes**. The expression of exogenously overexpressed mouse *Nfib* was examined by qPCR (A) and western blot (B). (C) *Nfib* overexpression and cellular localization was examined by immunostaining. Scale bar represents 25 μm and 50 μm for Pair 1 and 2, respectively. (D) The expression of putative NFIB target genes was validated by qPCR. Error bars represent mean ± SD.

Figure S6. Related to Figure 5. NFIB drives tumor dedifferentiation. (A and B) Tumor stained with NFIB and SYN, respectively (Control cohort). (C) Early lesions stained with CDH1 (Mycl cohort). (D-F) Tumor stained with CDH1, SYN and NFIB, respectively (Control cohort). (G-I)) Tumor stained with CDH1, NFIB and p44/42, respectively (Control cohort). Scale bars in (A-B) represent 100 μm. Scale bars in (C-I) represent and 500 μm.

Figure S7. Related to Figure 5. NFIB drives tumor dedifferentiation and invasion. (A) Lung from an animal taken 98 days following tumor induction (HE). (B and C) NFIB and Podoplanin (PDPN) staining indicating localization of NFIB positive cells in lymph vessels (arrowheads). (D) CDH1 staining of NE cells within lymph vessels (arrowheads). (E and F) NFIB staining of NE cells within lymph vessels and within extravascular/extrabronchial space (arrowheads). Early NFIB negative lesion is indicated with an arrow (Mycl cohort) (G-I) Lymphangiovascular invasion (LVI) within human

LCNEC tumor sample, HE, NFIB and CDH1, respectively. Scale bar in (A) represents 500 μm, in (B-E) 50 μm, in (F-I) 100 μm.

Table S1. Related to Figure 4. Commonly upregulated and downregulated genes following NFIB overexpression

Table S2. Related to Figure 6. Patient data and scoring of FFPE immunohistochemical preparations

Supplemental Experimental Procedures

Nfib inversion constructs

Two transcript variants of murine *Nfib* were cloned in the *pFrt-invCAG-ires-Luc* vector (Addgene, cat. no. 63576). Variant 1 was the full-length transcript of *Nfib* and variant 3 lacked the last three exons, 9 to 11 (Figure S1A). The *pFrt-invCAG-Nfib_v1-Luc* and *pFrt-invCAG-Nfib_v3-Luc* vectors contain the chicken β–actin (CAG) promoter followed by a lox71 site, an ATG-coding Frt site, a firefly Luciferase2 (*Luc*) gene with polyadenylation site in the opposite orientation, an internal ribosomal entry sequence (ires) sequence, the *Nfib* cDNA, and a lox66 site followed by three modules of splice acceptor:polyadenylation site also all in the opposite orientation of the promoter sequence (Figure S1C). After Flp-mediated integration of these vectors in the *Col1a1* locus they act as inversion transgenes that display conditional expression of the *Nifb* and *Luciferase* after Cre recombination (Figure S1D).

Genetic engineering in $Rb1^{F/F};Trp53^{F/F}$ ESCs and generation of mice

The ESC clone was co-transfected with three plasmids: one expressing Flp^e (pCAGGS-Flp^e, Open Biosystems, cat. no. MES4488), one expressing GFP (pCAG-GFP, Addgene, cat. no. 11150) and either one of the Flp-in vectors, i.e. *pFrt-invCAG-Nfib_v1-Luc* or *pFrt-invCAG-Nfib_v3-Luc*. Transfection efficiency was evaluated the next day by monitoring for green fluorescence. After 24 hours, Hygromycin-B (Gibo-Invitrogen, cat. no. 10687-010) was added and medium was refreshed every other day. Clones were picked after 14 days and screened for correct integration of the inversion construct by a PCR with a forward primer located in the CAG promoter, 5'-CTGCATCAGGTCGGAGACGCTGTCG-3' and the reverse primer in the Hygromycin-B gene, 5'-GGGTTCGGCTTCTGGCGTGTGACC-3'. Product size was 319 bp. Three clones were used to generate chimeric mice: 349_reESC_Nfib_v1 clone 1 and clone 4, and 349_reESC_Nfib_v3 clone 1. Chimeric mice from clone 1 of the Nfib_v1 and clone 1 of Nifb_v3 were used to establish a line by crossbreeding to $Rb1^{F/F};Trp53^{F/F}$ mice.

Experimental cohorts

$Rb1^{F/F};Trp53^{F/F}$ (Control cohort), *invCAG-Luc;*$Rb1^{F/F};Trp53^{F/F}$ (Control cohort), *invCAG-Mycl-Luc;*$Rb1^{F/F};Trp53^{F/F}$ (Mycl cohort) mice have been described earlier (Huijbers et al., 2014; Meuwissen et al., 2003). The latter two genotypes also contain an inversion construct in the *Col1a1* locus, one containing only the *Luc* gene and the other the *Mycl* gene, an ires sequence and the *Luc* gene, respectively. The Nfib cohort contains both *invCAG-Nfib_v1-Luc;*$Rb1^{F/F};Trp53^{F/F}$ *and invCAG-Nfib_v3-Luc;*$Rb1^{F/F};Trp53^{F/F}$ mice. The two Nfib genotypes were analyzed independently but merged, since no difference was observed between the two genotypes in survival and metatstasis. The Nfib/Mycl cohort was obtained by crossbreeding *invCAG-Nfib_v1-Luc;*$Rb1^{F/F};Trp53^{F/F}$ (from 349_reESC_Nfib_v1 clone 1) with *Mycl-Luc;*$Rb1^{F/F};Trp53^{F/F}$ mice. In the Nfib, Mycl and Control (Luc) cohorts, chimeric mice obtained after ESC injection were included in the experimental groups. The $Rb1^{F/F};Trp53^{F/F}$ mice in the Control cohort were littermate controls obtained by crossbreeding to either Nfib or Mycl Cohort mice. The various inversion transgenes were maintained heterozygous in all cohorts, though in the Nfib/Mycl cohort two different transgenes were present in the *Col1a1* locus.

Ethics statement

Mice were housed under standard conditions of feeding, light and temperature with free access to food and water. Male and female mice were represented equally in the experimental cohorts.

Tumor induction via intratracheal Ad5-CMV-Cre virus administration

Mice from the different cohorts were treated with cyclosporine A (Novartis) orally in the drinking water, 1 week prior to adenovirus administration and 2-3 weeks following infection. Viral Ad5-CMV-Cre particles (20 µl, 1 x 10^9; Gene Transfer Vector Core, University of Iowa) were injected intratracheally. Mice were monitored daily for signs of illness and culled upon respiratory distress or excessive weight loss (>20% of initial weight). A small number of experimental mice were culled at defined time points; 10, 14 and 20 weeks post viral infection.

Imaging of tumors

In vivo bioluminescence imaging was performed and quantified as described by Hsieh C. et al. 2005 (Hsieh et al., 2005) on a cryogenically cooled IVIS system (Xenogen Corp., CA, USA) using LivingImaging acquisition and analysis software (Xenogen). Luciferase units are photons/second x cm^2 x sr.

Histology, Immunohistochemistry, and Quantification

Tissues and organs were collected and fixed in EAF fixative (ethanol/acetic acid/formaldehyde/ saline at 40:5:10:45 v/v) and embedded in paraffin. Sections were prepared at 2 μm thickness from the paraffin blocks and stained with hematoxylin and eosin (HE) according to standard procedures. For immunohistochemistry (IHC), 4 um-thick sections were made on which antibodies were applied such as: Synaptophysin (Abcam, ab32127), NCAM (Chemicon, AB5032), CDH1 (Cell signaling, #3195), NFIB (Thermo Scientific, PA5-28299), CGRP (Sigma, C8198), Phospho-p44/42 (Cell Signaling, #4370). The sections were reviewed with a Zeiss Axioskop2 Plus microscope (Carl Zeiss Microscopy, Jena, Germany) and images were captured with a Zeiss AxioCam HRc digital camera and processed with AxioVision 4 software (both from Carl Zeiss Vision, München, Germany). For the quantification of liver metastasis, NCAM staining liver sections were analyzed using ImageJ software (National Institutes of Health).

Copy number analysis and qPCR analysis

Genomic DNA and total cellular RNA were simultaneously isolated from snap frozen tumor sample or normal lung tissue using the Allprep DNA/RNA/Protein mini kit (Qiagen) according to the manufacturer's instructions. Tissues were homogenized in RLT buffer using TissueLyser (Qiagen). The genomic DNA copy numbers for *Nfib* and *Mycl* were determined by using pre-designed Taqman copy number assays (Applied Biosystems). The probes of *Nfib* (Mm00128854_cn) and *Mycl* (Mm00558489_cn) were labeled with FAM and the Taqman copy number reference assay, mouse *Tert* (part #4458368) and mouse *Tfrc* (part #4458366) labeled with VIC were used for the internal reference copy number. Genomic DNA from normal lung tissue and mouse embryonic stem cells were used as normal controls. The cDNA equivalent to total RNA from same tumor sample was prepared using the Superscript II reverse transcriptase (Invitrogen) according to manufacturer's instructions. For real-time PCR, cDNA was subjected to 40 cycles of amplification using Taqman gene expression assays (Nfib, Mm01257775_m1 and Mm00616076_s1, Mycl, Mm00493155_m1) labeled with FAM and the pre-developed Taqman assay reagents of mouse beta actin (part #4352341) was used for normalization. For the validation of RNAseq gene expression analysis, total RNA from SCLC cells was extracted using RNeasy Mini Kit (Qiagen) and cDNA was prepared in same procedure as that for tumor samples. For real-time PCR, SYBR Green expression assay (Applied Biosystems) was performed with following primers (mouse Actin, 5'- aaatcgtgcgtgacatcaaa-3' and 5'-aaggaaggctggaaaagagg-3'; mouse Agt, 5'-tcaacacctacgttcacttcca-3' and 5'- gatcatgggcacagacacc-3'; mouse Chdh, 5'- cactgccttctcggctct-3' and 5'-tcctctatccaccgacagga-3'; mouse Clu, 5'-gatccaccaggctcaacag-3' and 5'-tgcggtcatcttcaccttc-3'; mouse Col4a1 5'-cgggagagaaaggtgctgt -3' and 5'- ctccaggcaagccatcaa -3'; mouse Itga 5'- atcctcctgagcgccttt -3' and 5'-tttcttctttagtggccttttga -3'; mouse Kcnma 5'- gtacctgtggaccgtttgct -3' and 5'- caccacctcctcttttttcgt -3'; mouse Pcsk6 5'-gactccagaagacgaggaagag -3' and 5'- acactcgggatggcacac -3'; mouse Ror1 5'-tgcaggggggaaatagaaaatc-3' and 5'-atggcgaactgagagcactt-3'; mouse Slc1a2 5'- gacgggatgaacgtcttaggt-3' and 5'- accatcagcttggcctgt-3'; mouse Sparc 5'-agaggaaacggtcgaggag-3' and 5'-ctcacacaccttgccatgtt-3' as per the manufacturer's instructions. The data from mouse Actin was used as normalization control.

***Nfib* splicing variants**

The cDNA from normal lung and tumor was used to examine the expression of full length *Nfib* (transcript variant 1) and *Nfib* transcript variant 3 lacking exon 9-11. To detect the full length *Nfib*, PCR primers designed from the *Nfib* exon 8 (mNfib_E8; 5'-tcaactcgaactccacctcc-3') to *Nfib* exon9 (mNfib_E9; 5'-gacaggtgtgaaatggccag-3') were used and the size of full length *Nfib* PCR product is 234bp. For the *Nfib* transcript variant 3, PCR primers designed from *Nfib* exon 8 (mNfib_E8) to exon 12 (mNfib_E12; 5'-aaaggaaccaagctagccca-3') of *Nfib* full length cDNA were used and the size of *Nfib* transcript variant 3 PCR product is 210bp. Phusion high fidelity PCR kit (New England Biolabs) was used for the amplification of *Nfib* splicing variants following the manufacturer's instructions.

DNA sequencing and Copy number profiling

The amount of double stranded DNA in genomic DNA samples was quantified using the Qubit® dsDNA HS Assay Kit (Invitrogen). Up to 250 ng of double stranded genomic DNA was fragmented by Covaris shearing to obtain fragment sizes of 160–180 bp. Samples were purified with the Agencourt AMPure XP PCR Purification beads according to manufacturer's instructions (Beckman Coulter, cat no A63881). DNA library preparation for Illumina sequencing was done with the TruSeq® DNA LT Sample Preparation kit (Illumina). The double-stranded DNA input amount was lower than advised by the Truseq protocol, so we used up to 250 ng of double-stranded DNA, such that 2.5 times less adapter concentration was used than prescribed in the TruSeq protocol. During enrichment PCR, 10 cycles were necessary to obtain enough yield for sequencing. All DNA libraries were analyzed on a BioAnalyzer system (Agilent Technologies) using the DNA7500 chips for determining the molarity. Up to ten

uniquely indexed samples were pooled equimolarly to give a final concentration of 10 nM. Pools were then sequenced using an Illumina HiSeq2000/2500 machine to coverage of 0.5×. This was done in one lane of a single-end 51 bp run according to manufacturer's instructions.
Reads were aligned to the reference genome (mm10) using the Burrows-Wheeler Aligner (BWA 7.10) (Li and Durbin, 2009). To obtain copy number profiles we use CopywriteR tool (Kuilman et al., 2015). The CopywriteR program was adapted for low coverage sequencing without peak calling algorithm. A depth-of-coverage method was used for 20-kb bins, and the read count was normalized for GC content and mappability. Log2-transformed ratios were calculated for all tumor samples versus reference (tail) sample. The normalized and corrected profiles were further analysed by circular binary segmentation (CBS) (Olshen et al., 2004). DNA copy number was visualized using the Broad Institute's Integrated Genome Viewer (http:// www.broadinstitute.org/igv).
Next-generation MPS Mate-pair libraries were prepared using the Nextera Mate Pair Sample Preparation Kit (Illumina, San Diego, CA, USA). Paired-end adapters were ligated to the fragments and the library was amplified by 18 cycles of PCR. Mate-pair libraries were subjected to 2 x 51 bases PES on a HiSeq 2000 (Illumina), following the manufacturers protocol. After adapter trimming the reads were aligned to the mm10 reference genome using BWA-MEM (version 0.7.5, http://arxiv.org/abs/1303.3997) (Stephens et al., 2011). Intrachromosomal rearrangements were detected by extracting paired reads that have a mapping quality > 50 for both ends and connect two locations that are at least 50kb apart. If two or more of those distinct read pairs are found within 30kb on both ends, the rearrangement is recorded.

Overexpression of NFIB in mouse SCLC cells
Cell lines from *invCAG-Mycl-Luc;Rb1$^{F/F}$;Trp53$^{F/F}$* (Mycl cohort) SCLC tumors were derived as previously described (Calbo et al., 2011). Cells were maintained in modified HITES medium DMEM/F12 (1:1) (GIBCO) supplemented with 4µg/ml Hydrocortisone (Sigma), 5 ng/ml murine EGF (Invitrogen), Insulin-Transferrin-Selenium mix/solution (GIBCO) and 10% Fetal Bovine Serum (GIBCO). For overexpression of NFIB, Myc-tagged ORF clone of mouse NFIB from Origene (MR206682) was excised and cloned into the pMSCV-puro retroviral vector (Invitrogen). Puromycin was used to select NFIB overexpressing cells. NFIB expression was validated by western blot and immunocytochemistry using antibody against NFIB (Thermo Scientific, PA5-28299) performed by standard procedures.

RNA-seq analysis
After quality filtering according to the illumina pipeline, 51-bp single-end reads were mapped to the mouse genome (mm10), using TopHat (2.0.12) (Trapnell et al., 2009). TopHat was run with default. Reads with mapping quality less than 10 and non-primary alignments were discarded. Remaining reads were counted using HTSeq-cout (Anders et al., 2015). Statistical analysis of the differential expression of genes was performed using DESeq2 (Love et al., 2014). Normalized read counts from DESeq2 are used to calculate the average fold change between each pairs (Table S1). Biological network analysis was performed using Ingenuity Pathway Analysis (IPA) (v 9.0, Ingenuity Systems, Mountain View, CA, USA) to predict potential biological processes, pathways and molecules affected by DEGs.

Human SCLC patient specimens
This study was approved by institutional review board of the NKI-AVL. We collected archived FFPE samples of 48 TC, AC, LCNEC and SCLC patients. The FFPE TC, AC, LCNEC and SCLC samples were primary and metastatic tumors diagnosed as stage I–IV tumors. All tumor samples were reviewed by at least two independent expert pathologists. The diagnosis was histomorphologically confirmed by H&E staining and immunohistochemistry.
Immunohistochemistry of the FFPE tumor samples was performed on a BenchMark Ultra autostainer (E-Cadherin) or Discovery Ultra autostainer(NFIB). Briefly, paraffin sections were cut at 3 µm, heated at 75°C for 28 minutes and deparaffinized in the instrument with EZ prep solution (Ventana Medical Systems). Heat-induced antigen retrieval was carried out using Cell Conditioning 1 (CC1, Ventana Medical Systems) for 32 minutes at 95^{0}C. E-cadherin was detected using NCH-38 (1/200 dilution, 32 minutes at 37^{0}C, Dako), NFIB was detected using a polyclonal antibody (Cat.No PA5-28299) (1/100 dilution, 32 minutes at 37^{0}C, ThermoScientific). E-Cadherin bound antibody was visualized using the Optiview Amplification kit (Ventana Medical Systems). Followed by the Optiview DAB detection kit (Ventana Medical systems). NFIB bound antibody was visualized using Anti-Rabbit HQ (Ventana Medical systems) for 12 minutes at 37^{0}C followed by Anti-HQ HRP (Ventana Medical systems) for 12 minutes at 37^{0}C, followed by the ChromoMap DAB detection kit (Ventana Medical Systems). Slides were counterstained with Hematoxylin II and Bluing Reagent (Ventana Medical Systems).

The H-score was determined by assessing the extent of nuclear immunoreactivity for NFIB and ECAD by KM and ES (Table S2). The score is obtained by the formula: 3 x percentage of strongly staining nuclei + 2 x percentage of moderately staining nuclei + percentage of weakly staining nuclei, giving a range of 0 to 300.
An experienced pathologist and KM scored the positive Mib-1 fraction by assessing the area with the highest positive fraction in the tumor. At 40X magnification the positive fraction was estimated by comparison to pictures with predefined positive fractions.
Overall survival was analyzed with the study cohort of 48 TC, AC, LCNEC and SCLC patients considering age of diagnosis, gender, tumor stage, treatment, smoking history and overall survival. This data was obtained by reviewing the electronic patients files of the NKI-AVL. If data was not available other hospitals were contacted for missing data (Table S2). The median follow-up time for this cohort of 48 TC, AC, LCNEC and SCLC patients was 38 months, and 42% of the patients were alive at the time of last follow-up.

Supplemental References

Anders, S., Pyl, P. T., and Huber, W. (2015). HTSeq--a Python framework to work with high-throughput sequencing data. Bioinformatics *31*, 166-169.
Calbo, J., van Montfort, E., Proost, N., van Drunen, E., Beverloo, H. B., Meuwissen, R., and Berns, A. (2011). A functional role for tumor cell heterogeneity in a mouse model of small cell lung cancer. Cancer cell *19*, 244-256.
Hsieh, C. L., Xie, Z., Liu, Z. Y., Green, J. E., Martin, W. D., Datta, M. W., Yeung, F., Pan, D., and Chung, L. W. (2005). A luciferase transgenic mouse model: visualization of prostate development and its androgen responsiveness in live animals. J Mol Endocrinol *35*, 293-304.
Huijbers, I. J., Bin Ali, R., Pritchard, C., Cozijnsen, M., Kwon, M. C., Proost, N., Song, J. Y., de Vries, H., Badhai, J., Sutherland, K.*, et al.* (2014). Rapid target gene validation in complex cancer mouse models using re-derived embryonic stem cells. EMBO molecular medicine *6*, 212-225.
Kuilman, T., Velds, A., Kemper, K., Ranzani, M., Bombardelli, L., Hoogstraat, M., Nevedomskaya, E., Xu, G., de Ruiter, J., Lolkema, M. P.*, et al.* (2015). CopywriteR: DNA copy number detection from off-target sequence data. Genome biology *16*, 49.
Li, H., and Durbin, R. (2009). Fast and accurate short read alignment with Burrows-Wheeler transform. Bioinformatics *25*, 1754-1760.
Love, M. I., Huber, W., and Anders, S. (2014). Moderated estimation of fold change and dispersion for RNA-seq data with DESeq2. Genome biology *15*, 550.
Meuwissen, R., Linn, S. C., Linnoila, R. I., Zevenhoven, J., Mooi, W. J., and Berns, A. (2003). Induction of small cell lung cancer by somatic inactivation of both Trp53 and Rb1 in a conditional mouse model. Cancer cell *4*, 181-189.
Olshen, A. B., Venkatraman, E. S., Lucito, R., and Wigler, M. (2004). Circular binary segmentation for the analysis of array-based DNA copy number data. Biostatistics *5*, 557-572.
Stephens, P. J., Greenman, C. D., Fu, B., Yang, F., Bignell, G. R., Mudie, L. J., Pleasance, E. D., Lau, K. W., Beare, D., Stebbings, L. A.*, et al.* (2011). Massive genomic rearrangement acquired in a single catastrophic event during cancer development. Cell *144*, 27-40.
Trapnell, C., Pachter, L., and Salzberg, S. L. (2009). TopHat: discovering splice junctions with RNA-Seq. Bioinformatics *25*, 1105-1111.